UNIVERSITÀ DEGLI STUDI DI MILANO

FACOLTÀ DI SCIENZE E TECNOLOGIE

Dipartimento di Fisica

Corso di Laurea Magistrale in Fisica

ELABORATO FINALE DI LAUREA

New estimates for Pinning Energies in neutron stars

Relatore: Professor Xavier Roca Maza
Correlatore: Professor Pierre M. Pizzochero
Correlatore: Dottor Enrico Vigezzi

Candidato:
Pietro Klausner
Matricola 939696

Anno Accademico 2020-2021

Contents

Introduction

Perhaps one of the most fascinating objects in the galaxy are neutron stars. They arise from the collapsing iron core of an exploding supernova, becoming a new, dense star. A typical neutron star mass is between one and two solar masses and its radius is of order of ten kilometers. The density at its center can be several times larger than the nuclear saturation density ($\rho_{sat} \sim 2.4 \times 10^{14}\,\mathrm{g/cm^3}$).

Of the many type of neutron stars, pulsars are rapid-rotating objects (their period can be as high as 10 s and as low as 1 ms) which emit very regular electromagnetic impulses. They are remarkably precise clocks, their stability rivalling that of atomic clocks.

Lots of observation show that pulsars slow down, due to their electromagnetic emissions. While this deceleration is steady, pulsars also exhibit sudden spin-ups, known as *glitches*. Such phenomenon was first observed in the late sixties, in Crab and Vela pulsars. While the relative growth in angular velocity is fairly small ($\Delta\Omega/\Omega \sim 10^{-6}$), the associated increase in angular momentum is quite remarkable.

It is still an open question which are the exact mechanisms that lead neutron stars to undergo such fascinating phenomena. The theoretical framework in which we set our work sees glitches as a macroscopic consequence of neutron superfluidity in the interior of the star. If this interpretation of the phenomenon is indeed correct, glitches would be the only observational evidence of the existence of a macroscopic superfluid inside a neutron star.

Somewhere between 300 m to 600 m beneath the surface, there lies the inner crust, where a lattice of neutron rich nuclei coexists with a sea of superfluid neutrons. In this region densities range from 2×10^{11} g/cm^3 (neutron drip density) to a fraction of the nuclear saturation density ρ_{sat}. While the lattice corotates with the star, the superfluid cannot simply do so.

One of the many peculiar feature of a superfluid is that, while it is immersed in a slowly rotating recipient, it cannot simply rotate with the system. Instead, the superfluid forms a lattice of vortices. A mean angular velocity, whose magnitude is proportional to the number of vortices on the surface of the recipient, can be defined. This happens also in neutron stars, where vortices thread the lattice of nuclei.

Clearly, it is crucial to understand the interaction between vortices and nuclei. If a force pins the vortices on a fixed position (whether on a nucleus or in between nuclei does not matter), the angular velocity of the superfluid cannot change. On the other hand, the crust does slow down.

Anderson and Itoh, in one of their works (Anderson and Itoh, 1975), recognized that the vortices experience also a force due to the Magnus effect. The Magnus force arises because the external superfluid exerts a different pressure

on the opposing sides of a vortex.

This force grows as the difference in angular velocity between the superfluid neutrons and the solid parts of the star increases. When a critical difference is reached, the vortices unpin from their sites and release the superfluid angular momentum to the crust, thus fuelling the glitch phenomenon.

To model the glitches, one would ideally estimate the forces acting on the vortices, namely the lift force and the force exerted by the lattice of nuclei. The latter is not straightforward to calculate. First, one should compute the microscopic force acting on a vortex respect to its position in the Wigner-Seitz cell of the lattice. This quantity is strongly dependent both on the density of the surrounding neutron sea and the nuclear physics input, since the nuclear interaction among neutrons and protons is not accurately known and some models must be used. Secondly, one should average this force over the length of a vortex line. Lastly one could compare this final quantity with the Magnus force to model glitches.

In this work we aim to improve on existing estimates of the microscopic interaction between a single vortex and its neighbouring nuclei. Computing directly the force acting on the vortex is a very complex task. In (Bulgac, Forbes, and Sharma, 2013), authors tried to compute directly this quantity, resorting to real-time dynamics.

It is common procedure instead to calculate a quantity called pinning energy: it is defined as the energy of the vortex respect to its position in the Wigner-Seitz cell. While there are different approaches in literature to compute this quantity (Epstein and Baym, 1988) (Donati and Pizzochero, 2006), we follow the method used by (Avogadro et al., 2008), which is a quantum self-consistent calculation.

In the first chapter we give a rapid overview on neutron stars, followed by a description of glitches and of their possible origin. We then discuss the main features of the inner crust and then introduce the cardinal quantity of this work, the *Pinning Energy*. We conclude with a brief summary of the previous estimates of this pinning energy in recent scientific literature.

In the second chapter we will explain in detail the computer code we use and how we can compute the pinning energy from its results. We will also discuss the modifications we implemented on the original code and show how they have impacted the results.

In the third chapter we will present our final results, giving our estimates of the pinning energies and comparing these new values with the ones reported in (Avogadro et al., 2008).

Finally, we will conclude our work with a summary and with some of the possible ways in which one could expand our research.

Chapter 1

Neutron stars

In the final life stage of a massive star (more than 8 solar masses), its core is a solar mass made of iron. Since two iron nuclei cannot undergo spontaneously the fusion process, the star crumbles under its own gravity. Inside the collapsing core, electrons are pushed inside the iron nuclei by the overwhelming pressure, thus turning protons into neutrons.

If the star mass is too big, eventually a black hole will be formed; otherwise the core will become a new neutron star.

Neutron stars have remarkable properties. They are approximately one solar mass ($\sim 1\ M_\odot$), with a radius of R $\sim$ 10 km. The densities in the core can reach values several time larger than the nuclear saturation density $\rho_{sat} \sim 2.4 \times 10^{14}\,\mathrm{g/cm^3}$. A neutron star is composed almost entirely by neutrons (up to 95%).

It is important for our discussion to understand the internal structure of a neutron star, which is displayed in Figure 1.1. A more detailed explanation can be found in Shapiro and Teukolsky (2004).

A thin atmosphere (some millimeters thick) of normal matter covers the surface of the star; the density in this region reaches $10^6\,\mathrm{g/cm^3}$.

Beneath it, one finds the outer crust, which is approximately 300 m deep. It is formed by a lattice of heavy nuclei which are in β-equilibrium with the surrounding relativistic degenerate electron gas. Density goes from $10^6\,\mathrm{g/cm^3}$ up to $4 \times 10^{11}\,\mathrm{g/cm^3}$.

Underneath the outer crust there's the inner crust, which is almost half a kilometer thick. In this region the density is so high that additional neutrons cannot be bound to the neutron rich nuclei; instead, a sea of superfluid neutrons coexists with a lattice of heavy nuclei. Density spans from $4 \times 10^{11}\,\mathrm{g/cm^3}$ (neutron drip density) to fractions of $\rho_{sat} \sim 2.4 \times 10^{14}\,\mathrm{g/cm^3}$, the nuclear saturation density.

The rest of the star is its core. Since the density keeps growing past ρ_{sat}, the concept of nucleus lose its meaning. Instead, there's a dense sea of neutrons, with a small concentration of superfluid protons and some electrons. In the most inner parts of the star there may be a region where exotic matter exists, e.g. neutron solid or quark matter. While this is a very fascinating topic, it's beyond the scope of this thesis and we will not explore it any further.

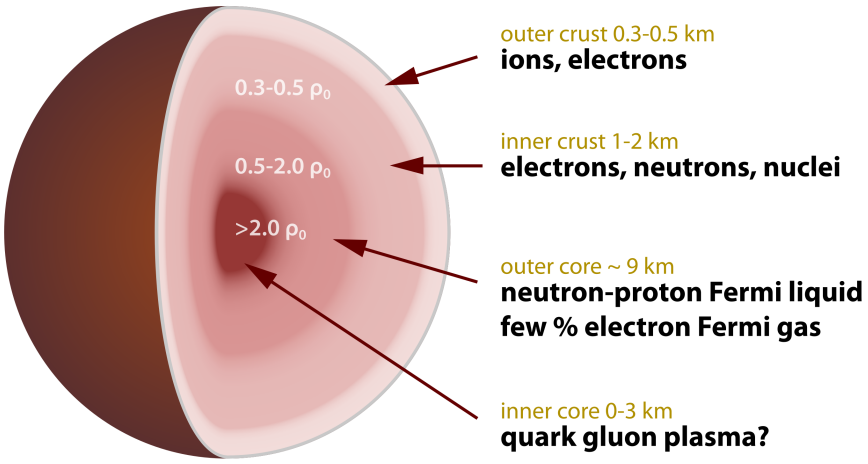

Figure 1.1: Internal structure of a neutron star. Picture taken from (*Wikipedia*).

1.1 Pulsars and Glitches

A handful of different types of neutron stars exists in the universe. One of particular interest to us are pulsars.

Pulsars emit electromagnetic pulses from a very narrow region, as represented in Figure 1.2; due to the rotation of the star, these pulses exhibit a periodic pattern and are on average very stable. Unfortunately, the mechanism which causes these emissions is not yet fully understood, and we will not engage in this matter. The most important feature of the pulses is that they are extremely regular, so much that some pulsar periods are known to a part in 10^{13}: the fastest stars spin around themselves in ~ 1 ms, while the slowest do it in ~ 10 s.

It is an observationally known fact that pulsars slow down with time, e.g. due to the magnetic fields emitting energy associated with rotation. While this is a steady deceleration, many sudden spin-ups have been detected by astronomers. In Figure 1.3 we report the period of the Vela pulsar over the years and we highlighted the spin-ups; in Table 1.1 we report instead observational data of these events for Vela and Crab pulsars (for more data on glitches, we refer to (Espinoza et al., 2011) and (*Pulsar glitches*)). These increases in the rotational speed are known as glitches and are central in our thesis work. As we can see from Table 1.1, the relative increase in angular velocity is quite modest, at best a part in a million.

It is essential to fully appreciate neutron star behaviour to investigate these fascinating phenomena. While small glitches can originate from earthquakes in the star's crust (also known as star-quakes), big ones may be a macroscopic consequence of the neutron superfluidity inside the star.

We will now focus on the inner crust and on how the neutron sea interacts with the lattice of heavy nuclei. First of all, it is a known fact that a superfluid contained in a rotating recipient cannot simply corotate with it, opposed to what a normal fluid would do. The superfluid velocity field is in fact irrotational, i.e.

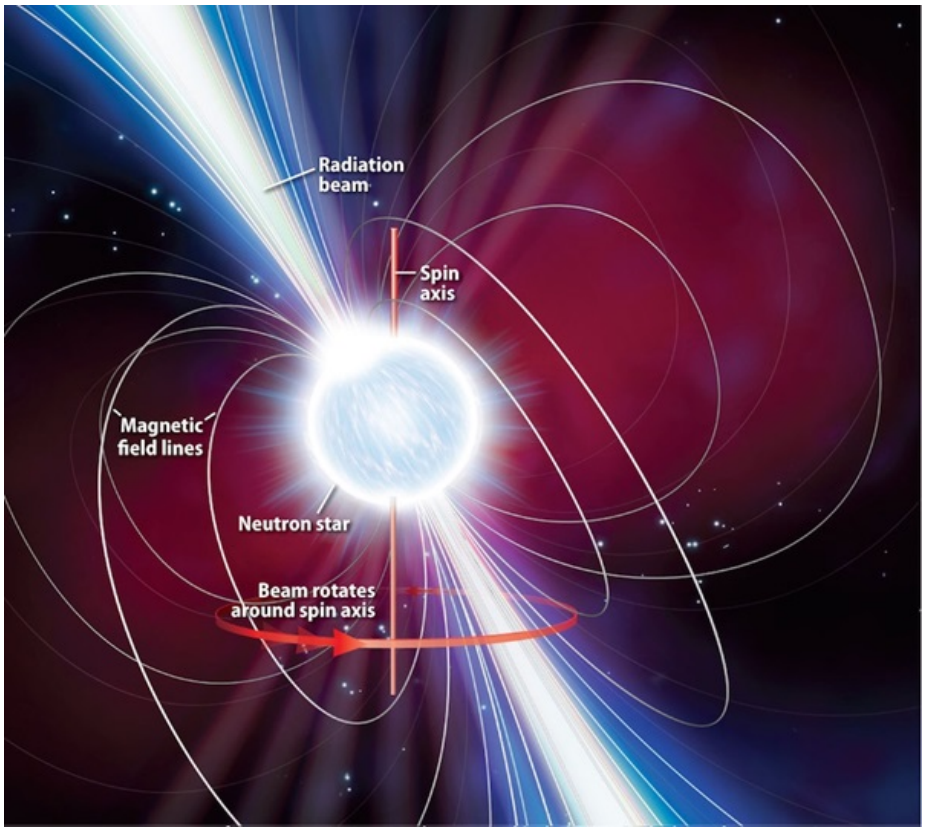

Figure 1.2: A pulsar. The light blue cone is the emitted electromagnetic pulse, while the white lines represent the star's magnetic field. The red vertical line is the star's axis of rotation. Picture taken from (*Discover*).

Date	Pulsar	Reference	$\Delta\Omega_0/\Omega_0$
3/1969	Vela	a	2.34×10^{-6}
8/1971	Vela	a	1.96×10^{-6}
12/1971	Vela	a	1.17×10^{-8}
10/1975	Vela	a	2.01×10^{-6}
7/1978	Vela	a	3.05×10^{-6}
10/1981	Vela	b	1.14×10^{-6}
9/1969	Crab	c	$\sim 10^{-8}$
10/1971	Crab	d	2×10^{-9}
2/1975	Crab	d	3.7×10^{-8}

Table 1.1: For each star, we show the date and the relative increase in angular velocity. This table is adapted from (Shapiro and Teukolsky, 2004). (a: (Downs, 1981) b: (McCulloch et al., 1981) c: (Boynton et al., 1972) d: (Lohsen, 1975))

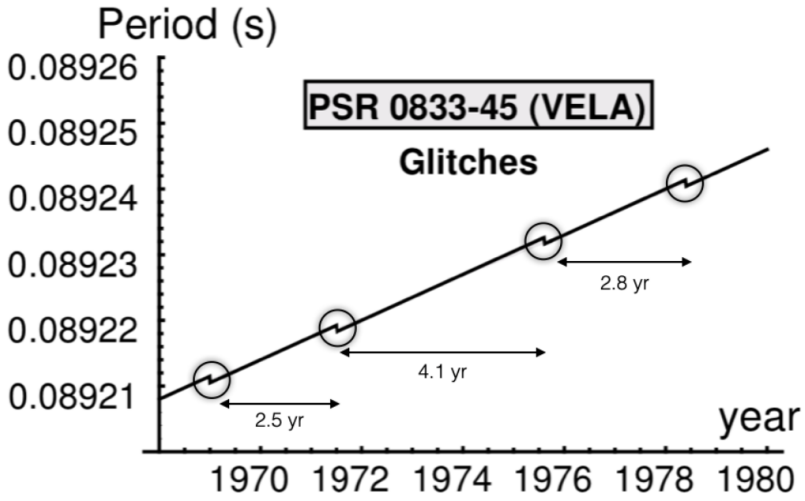

Figure 1.3: Period of the pulsar Vela over the course of a decade. The spin-ups, known as glitches and highlighted by small black circle, appear to happen regularly every ~ 3 years.

its rotor identically vanishes

$$\mathrm{rot}(\mathbf{v}_{\mathrm{sf}}) = 0 \tag{1.1}$$

Nonetheless, when the container exceed a critical angular speed, a mean velocity field with a non-null rotor can be defined, and, subsequently, a rotational velocity. The superfluid in the recipient forms an array of vortices parallel to the rotation axis (Lounasmaa and Thuneberg, 1999); the circulation around each vortex is quantized

$$\oint \mathbf{v} \cdot \mathbf{dl} = \frac{h}{2m_n} \tag{1.2}$$

where h is the Planck constant and m_n is the neutron mass. The condition (1.1) holds true everywhere except in the core of the vortex; if we average the fluid velocity over many vortex lines, we can obtain the usual relation

$$\mathrm{rot}\langle \mathbf{v} \rangle = 2\mathbf{\Omega}(r) \tag{1.3}$$

where

$$\mathbf{\Omega}(r) = \frac{h}{2m_n} \frac{N(r)}{\pi r^2} \tag{1.4}$$

$N(r)$ being the number of vortices in a radius r. The crucial aspect of this is that the superfluid angular velocity is tied to the density of vortex for unit area. Such density is related to the rotational speed of the recipient Ω_{Rec}

$$n_{vor} = \frac{4\Omega_{Rec} m_n}{h} \tag{1.5}$$

and, for the Crab pulsar, we have

$$n_{vor} \simeq 1.9 \times 10^5 \mathrm{cm}^2 \tag{1.6}$$

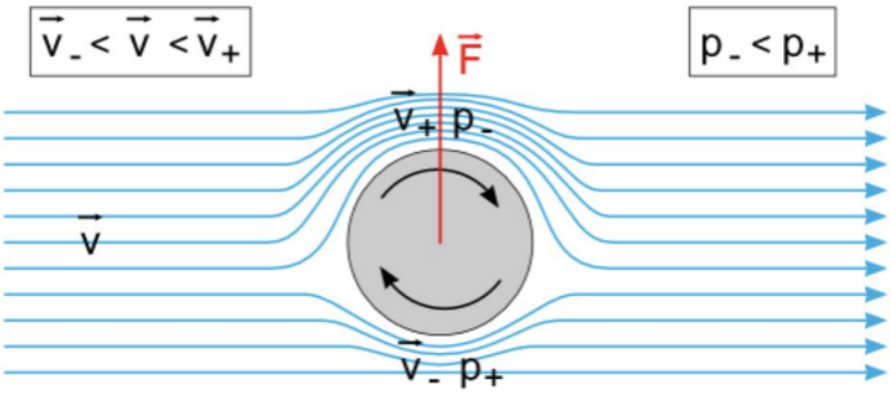

Figure 1.4: Representation of the Magnus effect. As a consequence of Bernoulli's principle, the velocity difference on the two sides of the vortex causes the pressure to be bigger where the velocity is smaller, thus giving rise to a force on the vortex. Picture taken from (*Magnus Effect*).

which means that the mean spacing between vortices d is

$$d = n_{vor}^{-1/2} \sim 10^{-2}\text{cm} \tag{1.7}$$

Therefore, vortices are a key aspect to the superfluid rotation, as they carry its angular momentum. In particular, glitches may be explained by the vortices interaction with the lattice of heavy nuclei inside the inner crust of a neutron star.

Due to this interaction, a vortex is either pinned on a nucleus (known as nuclear pinning configuration) or it is repelled by it (known as interstitial pinning configuration). Whichever the configuration, the vortex is kept fixed in place and cannot move. This freezes the angular speed of the superfluid, as the number of vortices cannot change, as we've discussed above. Therefore, while we observe the crust slow down, the superfluid neutrons in the inner crust cannot do so.

As pointed out by (Anderson and Itoh, 1975), vortices in the inner crust also experience a lift force, as they're moving in the neutron sea (Figure 1.4). We may express the force per unit length acting on a vortex as

$$\mathbf{F} = \frac{h}{2m_n}\rho_n \hat{\mathbf{z}} \times (\mathbf{v}_n - \mathbf{v}_v) \tag{1.8}$$

and the total force is calculated with an integration over the vortex length. Here, ρ_n is the density of the sea of neutrons, $\hat{\mathbf{z}}$ is the direction of the rotation axis, $\mathbf{v}_n$ is the velocity of the free neutrons and $\mathbf{v}_v$ is the speed of the vortices, which we may assume moving at the same speed of the crust.

As we see from (1.8), this force grows as the difference in angular velocity grows. When the difference in rotational velocity reaches a critical value, the vortices unpin from their position and release the neutrons angular momentum to the crust, thus generating the glitch phenomenon.

While one would ideally want to compute directly the force acting on each vortex, such a task would be extremely difficult. Instead, a simpler approach

is to compute a quantity called *Pinning Energy*. After a brief summary of the features of the inner crust, our discussion will focus on the pinning energy and on how to calculate it.

1.2 The inner crust

In a classical paper (Negele and Vautherin, 1973), Negele and Vautherin investigated the composition of the inner crust.

First, they found that the neutron excess respect to proton is indeed energetically convenient. As we can appreciate in Figure (1.5), the energy per particle in this configuration can be significantly lower than the energies of a β-stable uniform gas of electrons, protons and neutrons.

Hence, they divided the region in Wigner-Seitz's spherical cells, each with a nucleus at its center; half of the distance between two adjacent nuclei defines its radius R_{WS}. They investigated the composition of the inner crust at eleven different densities and determined the number of protons associated with the ground state and the radius of the Wigner-Seitz cell. These results are summarized in Table (1.2) and in Figure (1.6).

The authors did not include neutron or proton pairing in their calculations and neglected spin-orbit as well. Thus protons show important shell effects: in almost all cells, the proton number Z is either 40 or 50. The energies per particle of the two solutions are very close. In a recent work (Baldo et al., 2005), the same calculations has been performed, with and without proton pairing. Solutions with pairing are close in energy per particle to solutions without pairing, but predict a proton number Z spanning from 20 to 30; solutions without pairing found instead Z similar to (Negele and Vautherin, 1973).

In the present work, we will not calculate the favoured configuration, but simply assume the same proton numbers as determined by Negele and Vautherin. We will include neutron pairing, but we will neglect proton pairing and spin-orbit effects. In fact, we want to compare our results with those obtained in (Avogadro et al., 2008), who made the same assumptions.

As the density grows going deeper into the inner crust, the number of neutrons grows substantially, while the number of protons remains constant. Most importantly, the dimension of the W.S. cell shrinks notably: from $R_{WS} = 53.6$ fm at $n_b = 2.79 \times 10^{-4}\,\mathrm{fm}^{-3}$ to $R_{WS} = 14.4$ fm at $n_b = 7.89 \times 10^{-2}\,\mathrm{fm}^{-3}$. As we will see later, this has important consequences for our work.

1.3 The Pinning Energy

The question we aim to answer is how a vortex responds to the interaction of a nucleus next to it; in other words, we want to find the force acting on a vortex due to the presence of the nuclei nearby. This force is a force *per pinning site*.

In the inner crust, though, vortices are generally longer than the radius of the WS cells; therefore, as a vortex threads the lattice of nuclei, it interacts with many of them. The force *per pinning site* is needed to compute the force *per unit length* acting on a vortex, which is then needed to model the glitch phenomenon. A recent and beautiful paper (Seveso et al., 2016) describes well this procedure.

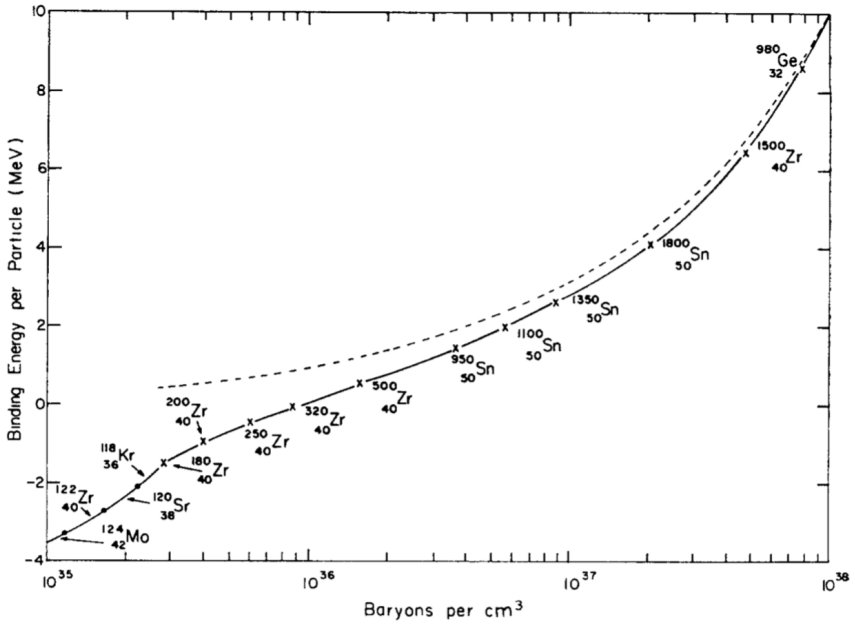

Figure 1.5: Binding energy per particle vs. baryonic density. The dotted line is the binding energy per particle for a uniform gas of protons, neutrons and electrons (from (Negele and Vautherin, 1973)).

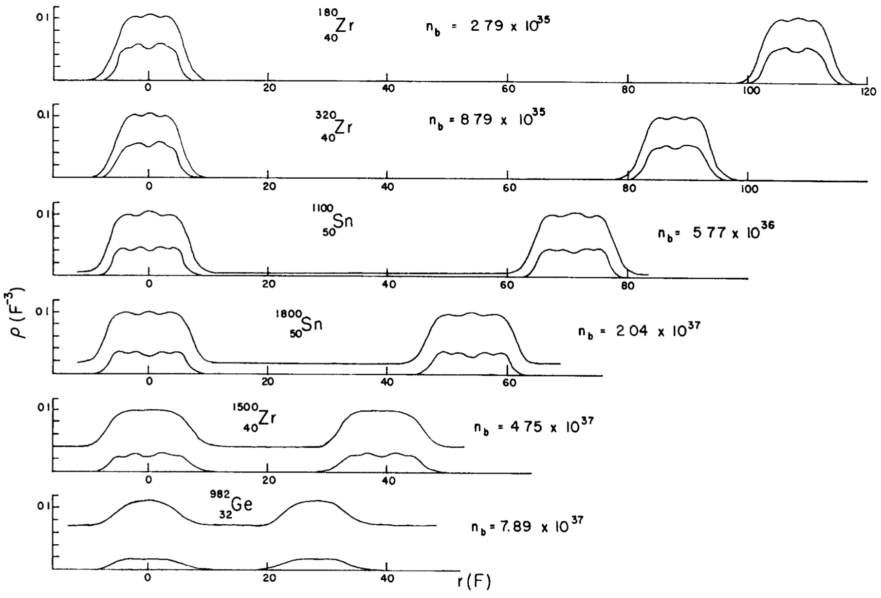

Figure 1.6: Density distribution of neutrons and protons along an axis connecting two cells, for six baryonic densities (from (Negele and Vautherin, 1973)).

$n_b\,[\mathrm{fm}^{-3}]$	N	Z	$\rho_n\,[\mathrm{fm}^{-3}]$	R_{WS} [fm]	$\tilde{x}$
2.79×10^{-4}	140	40	4.0×10^{-5}	53.60	0.53
4.00×10^{-4}	160	40	9.7×10^{-5}	49.24	0.53
6.00×10^{-4}	210	40	2.6×10^{-4}	46.33	0.53
8.79×10^{-4}	280	40	4.8×10^{-4}	44.30	0.53
1.59×10^{-3}	460	40	1.2×10^{-3}	42.19	0.52
3.73×10^{-3}	900	50	3.0×10^{-3}	39.32	0.46
5.77×10^{-3}	1050	50	4.7×10^{-3}	35.70	0.45
8.91×10^{-3}	1300	50	7.8×10^{-3}	33.07	0.44
2.04×10^{-2}	1750	50	1.84×10^{-2}	27.62	0.35
4.75×10^{-2}	1460	40	4.36×10^{-2}	19.61	0.28
7.89×10^{-2}	950	32	7.37×10^{-2}	14.38	0.16

Table 1.2: Numerical results of (Negele and Vautherin, 1973). n_b is the baryonic density, N and Z are respectively the number of neutrons and protons in each W.S. cell, ρ_n is the density of the neutron sea, R_{WS} is the radius of the Wigner-Seitz cell and $\tilde{x}$ is the protons to neutrons approximate ratio in the nuclei, which cannot be defined uniquely due to density fluctuations.

As we mentioned before, computing directly the force per pinning site is a complicated task. A simpler approach is to compute a quantity called Pinning Energy[1]. The pinning energy is the energy of the vortex-nucleus system as a function of distance between the axis of the vortex and the center of the nucleus. Once known, one could use it to easily derive the force between nucleus and vortex; however, computing such quantity is no simpler task than calculating directly the force.

Nonetheless, we can estimate the pinning energy recurring to a *mean* pinning energy. We define the mean pinning energy as the energy difference between the nuclear pinning configuration (NP, when the vortex is pinned on a nucleus) and the interstitial pinning (IP, when the vortex is pinned between nuclei at a distance R_{WS})

$$\langle E_p \rangle = E_{NP} - E_{IP} \tag{1.9}$$

The two configuration are illustrated in Figure (1.7). Once one has calculated such quantity, the force acting on a nucleus can be estimated as the module of the mean pinning energy divided by the typical distance of the system R_{WS}

$$\langle F_p \rangle = \frac{|E_p|}{R_{WS}} \tag{1.10}$$

and if $\langle E_p \rangle < 0$ the vortex is attracted by the nucleus; otherwise, if $\langle E_p \rangle > 0$, it is repelled by it.

It is then crucial to compute the pinning energy. In literature, several different methods have been explored.

First, we recall the work of Epstein and Baym (Epstein and Baym, 1988). Within the frame of the Ginzburg-Landau theory, they estimated the free energy of a nucleus near a vortex. They found that for densities bigger than $\rho \sim 10^{13}$

[1]To be exact, we want still to compute the pinning energy per pinning site, but for the sake of simplicity we will just call it pinning energy.

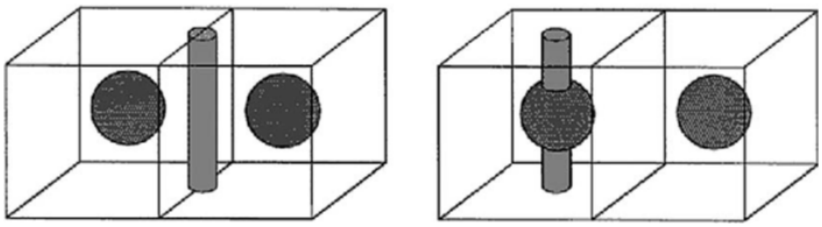

Figure 1.7: Interstitial pinning configuration and nuclear pinning configuration, as illustrated in (Donati and Pizzochero, 2004). In this work, the authors worked with cubical W.S. cells, with side $L_{WS} = 2R_{WS}$.

g/cm^3 (which roughly corresponds to 6×10^{-3} fm^{-3}) vortices indeed pin onto nuclei, while they are repelled for lower densities. However, the Ginzburg-Landau theory works at its best when the superfluid is close to its critical temperature. This does not hold for neutron stars; in fact, neutrons ar essentially at zero temperature ($T \sim 0.1$ MeV, while the critical temperature is $T_c \sim 0.5$ MeV).

Second, there are the already mentioned works of Pizzochero and Donati (Donati and Pizzochero, 2004) and (Donati and Pizzochero, 2006), where they used a semi-classical approximation for describing the vortex nucleus interaction, using a Thomas-Fermi model based on the local density approximation. They modeled the pairing gap with the realistic Argonne interaction; as the authors point out, though, the pairing gap should be suppressed by a factor β, which magnitude is uncertain. They presented they results for $\beta = 2$ and $\beta = 3$. Hence they found that pinning happens in a narrow density range, when $(2 \times 10^{13} < \rho < 5 \times 10^{13})$ g/cm^3.

Lastly, there is the paper of (Avogadro et al., 2008), which is a detailed microscopic study, based on the Hartree-Fock-Bogolyubov quantum mean field theory. A much more detailed discussion of this work will follow. They found modest nuclear pinning for small densities and interstitial pinning for higher densities.

We summarize the main results of these papers in Table (1.3).

Other authors (Bulgac, Forbes, and Sharma, 2013) used a different approach. Instead of resorting to the pinning energy, they used real-time dynamics within the time-dependent density functional theory to compute directly the force between vortex and nucleus. While it is not straightforward to compare their results with the one of the previously cited works, it is certainly an interesting approach that we mention for completeness.

In this work, we will try to find new estimates for the pinning energy; we will use and expand the computer code used in (Avogadro et al., 2008), as a self-consistent quantum calculation is the more direct and reliable approach.

In the next chapter we will explain in detail how the code works and what are the changes that we implemented.

n [fm^{-3}]	Epstein and Baym	Pizzochero and Donati		Vigezzi et al.	
		$\beta = 2$	$\beta = 3$	SkM*	SLy4
4.8×10^{-4}	4.4	0.81	0.21	-	-
1.0×10^{-3}	-	-	-	-1.51	-1.08
4.0×10^{-3}	-	-	-	-1.63	5.03
4.7×10^{-3}	-0.4	0.30	0.29	-	-
1.6×10^{-2}	-	-	-	7.97	6.21
1.8×10^{-2}	-15	-3.34	-2.74	-	-
3.8×10^{-3}	-	-	-	18.27	0.07
4.3×10^{-2}	-9	-1.79	-0.72	-	-
7.4×10^{-2}	-5.4	-0.06	-0.02	-	-

Table 1.3: Pinning energies from the cited works. n is the density of the surrounding neutron sea, while the energy is expressed in MeV. Negative values means nuclear pinning, while positive ones interstitial pinning.

Chapter 2

HFB and Code

As mentioned before, in this work we expand the work done in (Avogadro et al., 2008), where the authors solved Hartree-Fock-Bogolyubov (HFB) equations to investigate the behaviour of a vortex near a nucleus in the inner crust of a neutron star.

In this chapter we will first briefly discuss the theory behind the HFB equations. We will then give thorough description of the computer code used. Finally, we'll show the changes we implemented in the code and how they impacted the results.

2.1 Hartree Fock Bogolyubov equations

The HFB equations are a generalization of both the standard Hartree-Fock and BCS approximations, considering pairing correlation between nucleons as well as the nuclear mean field.

We will follow the presentation of the topic given in (Younes, Gogny, and Berger, 2019). The starting point to derive the equations is to consider a Bogolyubov transformation. A Bogolyubov transformation is a linear combination of a given set of creation a_i and annihilation operators $a_i^\dagger$

$$\begin{aligned} \eta_\mu^\dagger &= \sum_m \left(U_{m\mu} a_m^\dagger + V_{m\mu} a_m \right) \\ \eta_\mu &= \sum_m \left(U_{m\mu}^* a_m + V_{m\mu}^* a_m^\dagger \right) \end{aligned} \tag{2.1}$$

The relations (2.1) define a new set of operators, which are the quasi-particle creation and annihilation operators. We require these new operators to satisfy the standard fermion anti-commutation rules

$$\begin{aligned} \{\eta_\mu^\dagger, \eta_\nu^\dagger\} &= 0 \\ \{\eta_\mu, \eta_\nu\} &= 0 \\ \{\eta_\mu^\dagger, \eta_\nu\} &= \delta_{\mu,\nu} \end{aligned} \tag{2.2}$$

where $\delta_{\mu,\nu}$ is the Kronecker delta. Substituting (2.1) in (2.2), and remembering that the operators a_i and $a_i^\dagger$ satisfy the same anti-commutation rules, one finds these relations for the matrices U and V

$$\begin{aligned}\sum_m \left(U_{m\mu}U^*_{m\nu} + V_{m\mu}V^*_{m\nu}\right) &= \delta_{\mu,\nu} \\ \sum_m \left(U_{m\mu}V_{m\nu} + V_{m\mu}U_{m\nu}\right) &= 0\end{aligned} \tag{2.3}$$

Since the transformation (2.1) is unitary, we can write the inverse transformation

$$\begin{aligned}a^\dagger_m &= \sum_\mu \left(U^*_{m\mu}\eta^\dagger_\mu + V_{m\mu}\eta_\mu\right) \\ a_m &= \sum_\mu \left(U_{m\mu}\eta_\mu + V^*_{m\mu}\eta^\dagger_\mu\right)\end{aligned} \tag{2.4}$$

which then gives rise to relations analogous to (2.3)

$$\begin{aligned}\sum_\mu \left(U_{m\mu}U^*_{n\mu} + V_{m\mu}V^*_{n\mu}\right) &= \delta_{m,n} \\ \sum_\mu \left(U_{m\mu}V_{n\mu} + V_{m\mu}U_{n\mu}\right) &= 0\end{aligned} \tag{2.5}$$

First, we must define the vacuum state $\left|\tilde{0}\right\rangle$ respect to quasi-particles, i.e.

$$\eta_\mu \left|\tilde{0}\right\rangle = 0 \tag{2.6}$$

Then, given an hamiltonian of the form

$$H = \sum_{m,n} T_{mn} a^\dagger_m a_n + \frac{1}{4}\sum_{m,n,i,j} \bar{v}_{mnij} a^\dagger_m a^\dagger_n a_j a_i \tag{2.7}$$

where the term $\bar{v}_{mnij}$ is a compact notation for the antisymmetric matrix element

$$\bar{v}_{mnij} = \langle mn| \, v \, |ij - ji\rangle \tag{2.8}$$

we want to compute the its expected value of the energy E on the quasi-particle vacuum $\left|\tilde{0}\right\rangle$

$$E = \left\langle\tilde{0}\middle|H\middle|\tilde{0}\right\rangle \tag{2.9}$$

Since the Bogolyubov transformation is linear and $\left|\tilde{0}\right\rangle$ is still a vacuum state, (2.9) can be directly calculated with the aid of Wick theorem

$$\begin{aligned}\left\langle\tilde{0}\middle|a^\dagger_m a^\dagger_n a_j a_i\middle|\tilde{0}\right\rangle = &\left\langle\tilde{0}\middle|a^\dagger_m a_i\middle|\tilde{0}\right\rangle \left\langle\tilde{0}\middle|a^\dagger_n a_j\middle|\tilde{0}\right\rangle \\ &- \left\langle\tilde{0}\middle|a^\dagger_m a_j\middle|\tilde{0}\right\rangle \left\langle\tilde{0}\middle|a^\dagger_m a_i\middle|\tilde{0}\right\rangle \\ &+ \left\langle\tilde{0}\middle|a^\dagger_m a^\dagger_n\middle|\tilde{0}\right\rangle \left\langle\tilde{0}\middle|a_j a_i\middle|\tilde{0}\right\rangle\end{aligned} \tag{2.10}$$

Note that the quasi-particles vacuum is a superposition of states with different number of particles; thus terms such as $\left\langle\tilde{0}\middle|a^\dagger_m a^\dagger_n\middle|\tilde{0}\right\rangle$, which usually would be zero, now are non trivial.

We shall define two fundamental quantities: the *normal* density ρ

$$\rho_{im} = \left\langle\tilde{0}\middle|a^\dagger_m a_i\middle|\tilde{0}\right\rangle \tag{2.11}$$

and the *abnormal* density (or *pairing tensor*) κ

$$\kappa_{ji} = \langle\tilde{0}|a_j a_i|\tilde{0}\rangle \tag{2.12}$$

It is straightforward to see that ρ is a hermitian matrix and the tensor κ is antisymmetric

$$\begin{aligned} \rho_{mn} &= \rho^*_{nm} \\ \kappa_{mn} &= -\kappa_{nm} \end{aligned} \tag{2.13}$$

We can now rewrite (2.9) as

$$E = \sum_{m,n} T_{mn}\rho_{mn} + \frac{1}{2}\sum_{m,n,i,j} \bar{v}_{mnij}\rho_{im}\rho_{jn} + \frac{1}{4}\sum_{m,n,i,j} \bar{v}_{mnij}\kappa_{ji}\kappa^*_{nm} \tag{2.14}$$

The energy is thus a functional of the normal and abnormal density. It is worth noting that these two quantity can in turn easily be expressed in terms of the matrices U and V of the Bogolyubov transformation. Substituting in (2.11) and (2.12) the inverse transformation (2.4), gives

$$\begin{aligned} \rho_{mn} &= \sum_{\mu} V_{n\mu}V^*_{m\mu} \\ \kappa_{mn} &= \sum_{\mu} U_{m\mu}V_{n\mu} \end{aligned} \tag{2.15}$$

To find the HFB equations, we'll perform a variation on E respect to ρ and κ, on which the energy depends directly. We must also recognize that we have two constraints in the relations (2.3) and (2.5). It is easier to summarize such conditions using a new object, the generalized density matrix $\mathfrak{R}$, defined as

$$\mathfrak{R} = \begin{pmatrix} \mathfrak{R}^{11} & \mathfrak{R}^{12} \\ \mathfrak{R}^{21} & \mathfrak{R}^{22} \end{pmatrix} = \begin{pmatrix} \rho & -\kappa \\ \kappa^* & \mathbb{1} - \rho^* \end{pmatrix} \tag{2.16}$$

where $\mathbb{1}$ is the identity matrix. A straightforward calculation shows that (2.3) and (2.5) are equivalent to

$$\mathfrak{R}^2 = \mathfrak{R} \tag{2.17}$$

We can now proceed with the variation of the energy E. Beside the condition (2.17), we have two more constraints: the mean number of particles (neutron and protons) must be constant. We shall thus introduce the Lagrange multipliers λ_n, λ_p and Λ_{mn} so that the energy functional becomes

$$E(\rho,\kappa,\lambda_n,\lambda_p,\Lambda_{mn}) = E(\rho,\kappa) - \lambda_n\langle\tilde{0}|N_n|\tilde{0}\rangle - \lambda_p\langle\tilde{0}|N_p|\tilde{0}\rangle - \mathrm{Tr}[\Lambda(\mathfrak{R}^2 - \mathfrak{R})] \tag{2.18}$$

where the number operator N is defined by

$$N = \sum_i a^\dagger_i a_i$$

It is now easy to compute the variation respect to the elements of the generalized density matrix, which is equivalent to perform the variation respect to ρ and κ

$$\delta E(\rho,\kappa,\lambda_n,\lambda_p) = \sum_{i,j,m,n} \frac{\delta}{\delta\mathfrak{R}^{ij}_{mn}} E(\rho,\kappa,\lambda_n,\lambda_p)\delta\mathfrak{R}^{ij}_{mn} \tag{2.19}$$

This relation is equivalent to calculate the trace of

$$\delta E(\rho, \kappa, \lambda_n, \lambda_p) = \mathrm{Tr}(H\delta\mathfrak{R}) \tag{2.20}$$

where H is the Bogolyubov hamiltonian defined by

$$H^{ij}_{mn} = \sum_{i,j,m,n} \frac{\delta E(\rho, \kappa, \lambda_n, \lambda_p)}{\delta \mathfrak{R}^{ji}_{nm}} \tag{2.21}$$

Using the cycling property of the trace, we can variate (2.18) and find

$$\delta E(\rho, \kappa, \lambda_n, \lambda_p, \Lambda) = \mathrm{Tr}[H - (\Lambda\mathfrak{R} + \mathfrak{R}\Lambda - \Lambda)\delta\mathfrak{R}] \tag{2.22}$$

For this relation to hold, we must require that

$$H - (\Lambda\mathfrak{R} + \mathfrak{R}\Lambda - \Lambda) = 0 \tag{2.23}$$

Multiplying (2.23) on the right side by $\mathfrak{R}$ on the right side gives

$$H\mathfrak{R} - \mathfrak{R}\Lambda\mathfrak{R} = 0$$

If we then multiply (2.23) on the left by $\mathfrak{R}$ we get instead

$$\mathfrak{R}H - \mathfrak{R}\Lambda\mathfrak{R} = 0$$

Combining these two relation gives us the condition that H and $\mathfrak{R}$ must satisfy

$$[H, \mathfrak{R}] = 0 \tag{2.24}$$

that is, both H and $\mathfrak{R}$ can be diagonalized simultaneously.

We can now write explicitly the matrix element of H

$$\begin{aligned}
H^{11}_{mn} &= \frac{\delta E}{\delta \mathfrak{R}^{11}_{nm}} = \frac{\delta E}{\delta \rho_{nm}} = e_{mn} \\
H^{12}_{mn} &= \frac{\delta E}{\delta \mathfrak{R}^{21}_{nm}} = \frac{\delta E}{\delta \kappa^*_{nm}} = \Delta_{mn} \\
H^{21}_{mn} &= \frac{\delta E}{\delta \mathfrak{R}^{12}_{nm}} = -\frac{\delta E}{\delta \kappa_{nm}} = -\Delta^*_{mn} \\
H^{22}_{mn} &= \frac{\delta E}{\delta \mathfrak{R}^{22}_{nm}} = \frac{\delta E}{\delta(\delta_{m,n} - \rho^*_{nm})} = -\frac{\delta E}{\delta \rho^*_{mn}} = e^*_{mn}
\end{aligned} \tag{2.25}$$

where

$$\begin{aligned}
e_{mn} &= T_{mn} - \lambda_q \delta_{m,n}\delta_{q,q_m} + \sum_{ij} \bar{v}_{minj}\rho_{ij} \\
\Delta_{mn} &= \frac{1}{2}\sum_{ij} \bar{v}_{mnij}\kappa_{ji}
\end{aligned} \tag{2.26}$$

Resolving the diagonalization problem of H gives the HFB equations

$$\begin{pmatrix} e & \Delta \\ -\Delta^* & -e^* \end{pmatrix} \begin{pmatrix} U_\mu \\ V_\mu \end{pmatrix} = \varepsilon_\mu \begin{pmatrix} U_\mu \\ V_\mu \end{pmatrix} \tag{2.27}$$

where U_μ and V_μ are, respectively, the μ column of matrices U and V, which determines the quasi-particle creation operator $\eta^\dagger_\mu$. An important feature of (2.27) is that, since H is hermitian and thus its eigenvalues are real, for any given eigenvalue $\varepsilon_\mu > 0$, $\varepsilon_\mu < 0$ is also an eigenvalue with eigenvector

$$H\begin{pmatrix} V^*_\mu \\ U^*_\mu \end{pmatrix} = -\varepsilon_\mu \begin{pmatrix} V^*_\mu \\ U^*_\mu \end{pmatrix}$$

The matrix B that diagonalize H is then

$$B = \begin{pmatrix} U & V^* \\ V & U^* \end{pmatrix} \tag{2.28}$$

We have to control whether B also diagonalize $\mathfrak{R}$. From the definition of the generalized density matrix (2.16) and keeping in mind the Bogolyubov transformation (2.1), a straightforward calculation gives

$$B^\dagger \mathfrak{R} B = \begin{pmatrix} 0 & 0 \\ 0 & \mathbb{1} \end{pmatrix} \tag{2.29}$$

2.2 The vortex in HFB theory

As we will explain soon, the program we used expands the HFB equations on a particular single-particle basis. Hence we rewrite (2.27) as

$$\begin{cases} (h(\mathbf{x}) - \lambda)\, u_{qm}(\mathbf{x}) + \Delta(\mathbf{x}) v_{qm}(\mathbf{x}) = E_{qm} u_{qm}(\mathbf{x}) \\ \Delta^*(\mathbf{x}) u_{qm}(\mathbf{x}) - (h(\mathbf{x}) - \lambda)\, v_{qm}(\mathbf{x}) = E_{qm} v_{qm}(\mathbf{x}) \end{cases} \tag{2.30}$$

where $\mathbf{x}$ is the position in coordinate space; E_{qm} is the quasi-particle energy of level q with m being the projection of angular momentum on the z axis, while u_{qm}, v_{qm} are the amplitudes relative to that level. $h(\mathbf{x})$ is the single particle Hartree-Fock hamiltonian and $\Delta(\mathbf{x})$ is the pairing field.

We have yet to include the vortex in our description. The most natural approach is to work with cylindrical coordinates, i.e. $\mathbf{x} = (\rho, z, \varphi)$, since the presence of the vortex induces a symmetry around the z-axis. The explicit expression of the pairing field should then take the form (Gygi and Schlüter, 1991)

$$\Delta(\rho, z, \varphi) = \Delta(\rho, z)\, e^{i\nu\varphi} \tag{2.31}$$

where ν is the unit of angular momentum carried by the vortex. It is an observationally known fact that it is favorable for superfluids to form many vortices with one unit of angular momentum instead of one vortex with many units of angular momentum. Therefore, ν will be always set to one if the vortex is present.

The choice $\nu = 1$ implies that the Cooper pairs have a different character, as compared to the usual $\nu = 0$ pairing. In particular, the paired levels must have different parity. As a consequence, nuclear shell effects act in a quite different way on the $\nu = 1$ gap, as compared $\nu = 0$. This point is discussed at length in (Avogadro et al., 2008).

We solve (2.30) via an iterative process, both for protons and neutrons, with an adequate chemical potential λ for each. The density is then calculated as

$$n(\rho, z, \varphi) = \sum_{qm} |v_{qm}(\rho, z, \varphi)|^2 \tag{2.32}$$

while the abnormal density is

$$\kappa(\rho, z, \varphi) = \sum_{qm} u_{qm}(\rho, z, \varphi) v_{qm}(\rho, z, \varphi)^* \tag{2.33}$$

From the normal and abnormal densities we then calculate new potentials which in turn will be used to construct new HFB equations (2.30). The single-particle Hartree-Fock hamiltonian h is composed of a kinetic term T and a potential term U_{HF}. The latter is computed from a Skyrme-like force and it is density dependent, while the former includes the correction for the effective mass m^* from the same interaction,

$$T = -\nabla \left(\frac{\hbar^2}{2m^*(\rho, z, \varphi)} \nabla \right)$$

The pairing field has the explicit form

$$\Delta(\rho, z, \varphi) = -V_{pair} \kappa(\rho, z, \varphi)$$

where V_{pair} is an appropriate potential. For it to have the same φ-dependence of (2.31), we then require that the amplitudes u and v to be

$$\begin{aligned} u_{qm}(\rho, z, \varphi) &\propto e^{im\varphi} \\ v_{qm}(\rho, z, \varphi) &\propto e^{i(m-\nu)\varphi} \end{aligned} \tag{2.34}$$

We observe also that $n(\rho, z, \varphi) = n(\rho, z)$; the density and all the density-dependent quantities have therefore an azimuthal symmetry.

2.3 Interactions

We will now discuss in detail the choice for the potential V_{pair} and the hamiltonian h.

2.3.1 Skyrme Interaction

As mentioned before, we use a Skyrme-like interaction to write the single-particle hamiltonian $h(\mathbf{x}) = h(\rho, z, \varphi)$ in (2.30).

Given two nucleons in position $\mathbf{r}_1$ and $\mathbf{r}_2$, the standard form of the Skyrme-force is

$$\begin{aligned} V(\mathbf{r}_1, \mathbf{r}_2) = & \, t_0 \left(1 + x_0 P_\sigma\right) \delta(\mathbf{r}) \\ & + \frac{1}{2} t_1 \left((1 + x_1 P_\sigma) \right) \left[\mathbf{P}'^2 \delta(\mathbf{r}) + \mathbf{P}^2 \delta(\mathbf{r}) \right] \\ & + t_2 \left((1 + x_2 P_\sigma) \right) \mathbf{P}' \delta(\mathbf{r}) \mathbf{P} \\ & + \frac{1}{6} t_3 \left((1 + x_3 P_\sigma) \right) \rho^\alpha(\mathbf{R}) \delta(\mathbf{r}) \\ & + i W_0 \boldsymbol{\sigma} \left[\mathbf{P}' \times \delta(\mathbf{r}) \mathbf{P} \right] \end{aligned} \tag{2.35}$$

where $\mathbf{r} = \mathbf{r}_1 - \mathbf{r}_2$, $\mathbf{R} = \frac{1}{2}(\mathbf{r}_1 + \mathbf{r}_2)$, $\mathbf{P} = \frac{1}{2i}(\nabla_1 - \nabla_2)$, $\mathbf{P}'$ is c.c. of $\mathbf{P}$ acting on the left, $\boldsymbol{\sigma} = \boldsymbol{\sigma}_1 + \boldsymbol{\sigma}_2$ and $P_\sigma = (1 + \boldsymbol{\sigma}_1 \cdot \boldsymbol{\sigma}_2)/2$.

Following from (2.35), within the HF approximation, one can obtain an explicit expression for the self-consistent potential

$$h(\mathbf{x}) = -\nabla \frac{\hbar^2}{2m_q^*(\mathbf{x})} \nabla + U_q(\mathbf{x}) + \delta_{q,p} V_C - i\mathbf{W}_q(\mathbf{x}) \cdot (\nabla \times \sigma) \tag{2.36}$$

where q can stand for p (protons) or n (neutrons).

Remembering that n_q, τ_q and J_q are the density, the kinetic density and the spin-density of either protons or neutrons, and that $n = n_p + n_n$, $\tau = \tau_p + \tau_n$ and $J = J_p + J_n$, we write the terms in (2.36) following (Chabanat et al., 1997), (Chabanat et al., 1998a) and (Chabanat et al., 1998b).

The effective mass m_q^* is

$$\begin{aligned} \frac{\hbar^2}{2m_q^*(\mathbf{x})} = \frac{\hbar^2}{2m_q} &+ \frac{1}{8}\Big[t_1(2+x_1) + t_2(2+x_2)\Big] n(\mathbf{x}) \\ &- \frac{1}{8}\Big[t_1(1+2x_1) + t_2(1+2x_2)\Big] n_q(\mathbf{x}) \end{aligned} \tag{2.37}$$

the self-consistent potential U_q reads

$$\begin{aligned} U_q(\mathbf{x}) = &\frac{1}{2} t_0 \Big[(2+x_0)n + (1+2x_0)n_q\Big] \\ &+ \frac{1}{24} t_3 \Big\{(2+x_3)(2+\alpha) n^{\alpha+1} - (2x_3+1)\left[2n^\alpha n_q + \alpha n^{\alpha-1}(n_p^2 + n_n^2)\right]\Big\} \\ &+ \frac{1}{8}\Big[t_1(2+x_1) + t_2(2+x_2)\Big]\tau + \frac{1}{8}\Big[t_2(1+2x_2) - t_1(1+2x_1)\Big]\tau_q \\ &+ \frac{1}{16}\Big[t_2(2+x_2) - 3t_1(2+x_1)\Big]\nabla^2 n \\ &+ \frac{1}{16}\Big[t_2(1+2x_2) + 3t_1(1+2x_1)\Big]\nabla^2 n_q \\ &- \frac{1}{2} W_0 \Big[\nabla \cdot \mathbf{J} + \nabla \cdot \mathbf{J}_q\Big] \end{aligned} \tag{2.38}$$

while the spin-orbit field is

$$\mathbf{W}_q(\mathbf{x}) = \frac{1}{2} W_0 (\nabla n + \nabla n_q) + \frac{1}{8}(t_1 - t_2)\mathbf{J}_q - \frac{1}{8}(t_1 x_1 + t_2 x_2)\mathbf{J} \tag{2.39}$$

Lastly, the Coulomb potential, with the Slater approximation for the exchange part, reads

$$V_C(\mathbf{x}) = e^2 \left(\int \frac{n_p(\mathbf{x}')\mathrm{d}_3 x'}{|\mathbf{x} - \mathbf{x}'|} - \left(\frac{3}{\pi}\right)^{1/3} n_p(\mathbf{x})^{1/3} \right) \tag{2.40}$$

In the code, we neglect the spin-orbit interaction, taking into account the spin simply with a degeneracy factor $g = 2$. As a consequence, $J = 0$ identically, and its contributions to the potentials are therefore null; we decided to include it in our discussion for completeness.

Each term of the potentials contributes to a term of the energy density of the system $\mathcal{H}_{\mathcal{HF}}(\mathbf{x})$, which in turn is subdivided in different components

$$\mathcal{H}_{\mathcal{HF}} = \mathcal{K} + \mathcal{H}_0 + \mathcal{H}_3 + \mathcal{H}_{eff} + \mathcal{H}_{fin} + \mathcal{H}_C \tag{2.41}$$

where each term reads

$$\begin{aligned}
\mathcal{K} &= \frac{\hbar^2}{2m}\tau \\
\mathcal{H}_0 &= \frac{1}{4}t_0\Big[(2+x_0)n^2 - (2x_0+1)(n_p^2+n_n^2)\Big] \\
\mathcal{H}_3 &= \frac{1}{24}t_3 n^\alpha\Big[(2+x_3)n^2 - (2x_3+1)(n_p^2+n_n^2)\Big] \\
\mathcal{H}_{eff} &= \frac{1}{8}\Big[t_1(2+x_1) + t_2(2+x_2)\Big]\tau n \\
&\quad + \frac{1}{8}\Big[t_2(2x_2+1) - t_1(2x_1+1)\Big](\tau_p n_p + \tau_n n_n) \\
\mathcal{H}_{fin} &= \frac{1}{32}\Big[3t_1(2+x_1) - t2(2+x_2)\Big](\nabla n)^2 \\
&\quad - \frac{1}{32}\Big[3t_1(2x_1+1) + 3t_2(2x_2+1)\Big]\Big[(\nabla n_p)^2 + (\nabla n_n)^2\Big] \\
\mathcal{H}_C &= e^2\left(\frac{n_p}{2}\int\frac{n_p(\mathbf{x}')\mathrm{d}_3x'}{|\mathbf{x}-\mathbf{x}'|} - \frac{3}{4}\left(\frac{3}{\pi}\right)^{1/3} n_p(\mathbf{x})^{4/3}\right)
\end{aligned} \tag{2.42}$$

We omitted the spin-originated terms in the expression.

2.3.2 The Pairing potential

For the pairing interaction, we chose a density dependent, contact potential of the form

$$V_{pair}(\mathbf{x},\mathbf{x}') = V_0\left(1 - \eta\left(\frac{n(\mathbf{x})}{0.08}\right)^a\right)\delta(\mathbf{x}-\mathbf{x}') \tag{2.43}$$

where $V_0 = -481$ MeV $\cdot$ fm^{-3}, $\eta = 0.7$ and $a = 0.45$; these parameters reproduce the pairing gap of uniform neutron matter, obtained with a realistic nucleon-nucleon interaction (Garrido et al., 1999). In Figure 2.1 the pairing gap of uniform neutron matter obtained with (2.43) as a function of its Fermi momentum. As a comparison, we show also the gap obtained with a realistic Argonne interaction. Since interaction (2.43) has a contact nature, it is necessary to introduce an energy cutoff E_{cut}. For our calculations, we have chosen $E_{cut} = 60$ MeV.

Finally, the presence of the pairing field gives rise to an additional contribution to the energy density

$$\mathcal{H}_{pair} = -\frac{1}{2}\kappa^*\Delta \tag{2.44}$$

so that the total energy density in

$$\mathcal{H}_{tot} = \mathcal{H}_{\mathcal{HF}} + \mathcal{H}_{pair} \tag{2.45}$$

Hence the total energy E of the system is the volume integral of $\mathcal{H}$

$$E_{tot} = \int_V \mathrm{d}_3x\ \mathcal{H}(\mathbf{x}) \tag{2.46}$$

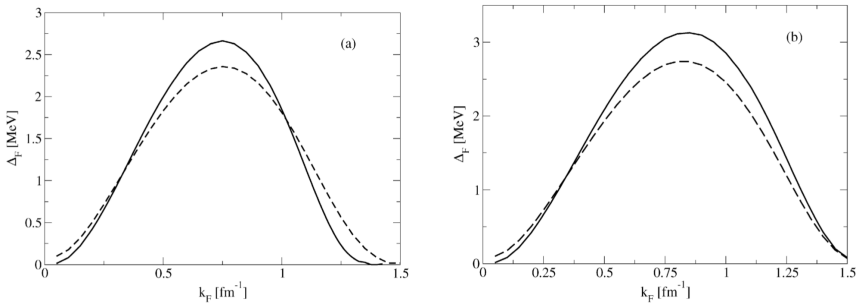

Figure 2.1: Pairing gap obtained with (2.43) (dashed curve), for different Fermi momenta k_F, compared with the one obtained from a realistic Argonne interaction (solid curve). In (a) the single particle levels have been calculated with the SLy4 interaction, whilst in (b) with the SkM* interaction. This figure was taken from (Avogadro et al., 2008).

2.4 Numerical Details

We solve (2.30) in a cylindrical box with height h_{box} and radius ρ_{box}. As mentioned before, we search a solution expanded on a single-particle basis, so that the amplitudes $u_{qm}(\rho, z, \varphi)$ and $v_{qm}(\rho, z, \varphi)$ for the quasi-particle level q with projection of angular momentum along the z-axis m are

$$\begin{aligned} u_{qm}(\rho, z, \varphi) &= \sum_{nl} U^{nl}_{qm} f_{nm}(\rho) g_l(z) e^{im\varphi} \\ v_{qm}(\rho, z, \varphi) &= \sum_{nl} V^{nl}_{qm} f_{nm-\nu}(\rho) g_l(z) e^{i(m-\nu)\varphi} \end{aligned} \tag{2.47}$$

On the ρ axis, functions $f_{nm}(\rho)$ are the solution of the Schrödinger equation for free particles

$$-\frac{\hbar^2}{2m_0}\left(\frac{1}{\rho}\frac{\partial}{\partial\rho}\left(\rho\frac{\partial}{\partial\rho}\right) + \frac{m^2}{\rho^2}\right) f_{nm}(\rho) = e_{nm} f_{nm}(\rho) \tag{2.48}$$

where m_0 is the bare nucleon mass and the index n is the number of nodes of function $f_{nm}(\rho)$ on the ρ axis.

On the z axis, functions $g_l(z)$ are normalized plane waves

$$g_l(z) = \sqrt{\frac{2}{h_{box}}} \sin\left(k_l\left(z + \frac{h_{box}}{2}\right)\right),\ k_l = \frac{\pi}{h_{box}}, \frac{2\pi}{h_{box}}, \ldots \tag{2.49}$$

so that we have

$$\begin{aligned} -\frac{\hbar^2}{2m_0}\left(\frac{\partial^2}{\partial z^2} + \frac{1}{\rho}\frac{\partial^2}{\partial\varphi^2} + \frac{1}{\rho}\frac{\partial}{\partial\rho}\left(\rho\frac{\partial}{\partial\rho}\right)\right) f_{nm}(\rho) g_l(z) e^{im\varphi} = \\ \left(e_{nm} + \frac{\hbar^2 k_l^2}{2m_0}\right) f_{nm}(\rho) g_l(z) e^{im\varphi} \end{aligned} \tag{2.50}$$

As for the boundary condition, each single-particle function vanishes at the edge of the box.

To solve (2.30), we project it onto generic basis states $|m,n,l\rangle$. Therefore our system of equation becomes, in matrix form

$$\begin{pmatrix} \langle m_2,n_2,l_2|h-\lambda|m_1,n_2,l_2\rangle & \langle m_2,n_2,l_2|\Delta|m_1,n_2,l_2\rangle \\ \langle m_2,n_2,l_2|\Delta^*|m_1,n_2,l_2\rangle & -\langle m_2,n_2,l_2|h-\lambda|m_1,n_2,l_2\rangle \end{pmatrix} \tag{2.51}$$

Since h depends only on the density, and the density does not depend on the azimuthal angle φ, it holds

$$\langle m_2,n_2,l_2|h|m_1,n_1,l_1\rangle = \delta_{m_1,m_2}\langle n_2,l_2|h|n_1,l_1\rangle \tag{2.52}$$

On the other hand, $\Delta = \Delta(\rho,z)e^{i\nu\varphi}$. It follows

$$\langle m_2,n_2,l_2|\Delta(\rho,z)e^{i\nu\varphi}|m_1,n_1,l_1\rangle = \delta_{m_1,m_2+\nu}\langle n_2,l_2|\Delta(\rho,z)|n_1,l_1\rangle \tag{2.53}$$

We can now rewrite (2.30) explicitly. From (2.36) and (2.31), we find

$$\begin{cases} \sum_{n_2l_2}\left(h^m_{n_1l_1n_2l_2}-\lambda\right)U^{qm}_{n_2l_2} + \Delta^m_{n_1l_1n_2l_2}V^{qm}_{n_2l_2} & = E^{qm}U^{qm}_{n_1l_1} \\ \sum_{n_2l_2}\Delta^m_{n_1l_1n_2l_2}U^{qm}_{n_2l_2} - \left(h^m_{n_1l_1n_2l_2}-\lambda\right)V^{qm}_{n_2l_2} & = E^{qm}V^{qm}_{n_1l_1} \end{cases} \tag{2.54}$$

where

$$\begin{aligned} h^m_{n_1l_1n_2l_2} = 2\pi\int_0^{h_{box}} 2\mathrm{d}z \int_0^{\rho_{box}} \rho\,\mathrm{d}\rho \quad \cdot \\ \Bigg\{ f_{n_2m}(\rho)g_{l_2}(z)\left(U(\rho,z)+\left(\frac{m_0}{m^*(\rho,z)}\right)\left(e_{n_1m}+\frac{\hbar^2k_{l_1}^2}{2m_0}\right)-\lambda\right)f_{n_1m}(\rho)g_{l_1}(z) \\ +f_{n_2m}(\rho)g_{l_2}(z)\left(\frac{\partial}{\partial\rho}\left(\frac{\hbar^2}{2m^*(\rho,z)}\right)\cdot\frac{\partial f_{n_1m}(\rho)}{\partial\rho}\right)g_{l_1}(z) \\ +f_{n_2m}(\rho)g_{l_2}(z)\left(\frac{\partial}{\partial z}\left(\frac{\hbar^2}{2m^*(\rho,z)}\right)\cdot\frac{\partial g_{l_1}(z)}{\partial z}\right)f_{n_1m}(\rho)\Bigg\} \end{aligned} \tag{2.55}$$

and

$$\begin{aligned} \Delta^m_{n_1l_1n_2l_2} = 2\pi\int_0^{h_{box}} 2\mathrm{d}z \int_0^{\rho_{box}} \rho\,\mathrm{d}\rho \quad \cdot \\ \left(f_{n_2m-\nu}(\rho)g_{l_2}(z)\Delta(\rho,z)f_{n_1m}(\rho)g_{l_1}(z)\right) \end{aligned} \tag{2.56}$$

Since protons and neutrons have different self-potentials (2.38), they give rise to two different systems (2.54). From the solution of such systems we can then compute new densities, from which in turn we can use to have new equations (2.54). This iterative process stops once the relative energy difference between subsequent iterations is lower than an appropriate value.

Since protons are confined in the nucleus, the dimension of their box is smaller, fixed at 15 fm: so that it's big enough to contain all the protons, but small enough to shorten the calculation times.

We follow different criteria for choosing the chemical potential λ of neutrons and protons: for the former, it's chosen to give the asymptotic density of the

neutron sea, as in Table 1.2; for the latter, the number of particles Z is fixed from input and an algorithm adjusts λ_p to give the adequate number of protons in each cell.

In (Negele and Vautherin, 1973), the authors found that the optimal values of Z are either 40 or 50, excluding the highest density in Table 1.2.Both solutions are very close in energy per particle. They did not consider proton pairing, so that protons are close to shell closure. Beside neglecting proton pairing, we do not consider the spin-orbit interaction either. As a consequence, we find shell closure at either $Z = 40$ or $Z = 58$. We choose to set $Z = 40$ for each of our calculations.

Finally, since we do not consider proton pairing, there cannot be a proton-vortex and ν for protons is always zero.

2.5 Binding and pinning energy

As stated before, the pinning energy is the microscopic energy of the vortex-nucleus system in the inner crust of the star; ideally, one would like to know such energy for each separation distance $0 < \rho < R_{WS}$ between the axis of the vortex and center of the nucleus, where R_{WS} is the dimension of the spherical Wigner-Seitz cell. To do so, we should solve the HFB equations in a WS cell where there are present, simultaneously, both a vortex and a nucleus; hence we should study the energy of the system as a function of the separation distance between the two.

Unfortunately, the numerical method we have described in this chapter does not allow to perform such calculation, mainly for two reasons. First, for any non zero distance between the vortex axis and the center of the nucleus, the rotational symmetry around the z-axis would be broken, making the actual computation very difficult. Second, R_{WS} becomes quite small as the neutron-sea density rises, so that the vortex could cross over neighbouring WS cells. It would then be necessary to account for the interaction between the vortex and the other nuclei in the lattice.

However, as explained in Section 1.3, we can compute a mean pinning energy $\langle E_p \rangle$, from which modelling neutron star glitches. For the sake of simplicity, we will refer to the mean pinning energy $\langle E_p \rangle$ as the pinning energy E_p.

We solve the HFB equations (2.54) in four different configurations and, by comparing the total energies of each situation, we can compute the *binding* energy of the vortex onto the nucleus. The four configurations are:

neutron sea (NS): the neutron sea, with neither a nucleus ($Z = 0$) nor a vortex ($\nu = 0$);

nucleus (Nu): a nucleus ($Z \neq 0$) with no vortex vortex ($\nu = 0$), surrounded by the neutron sea;

interstitial pinning (IP): a vortex ($\nu = 1$) with no nucleus ($Z = 0$), surrounded by the neutron sea;

nuclear pinning (NP): a nucleus ($Z \neq 0$) and a vortex ($\nu = 1$) on top of it, surrounded by the neutron sea.

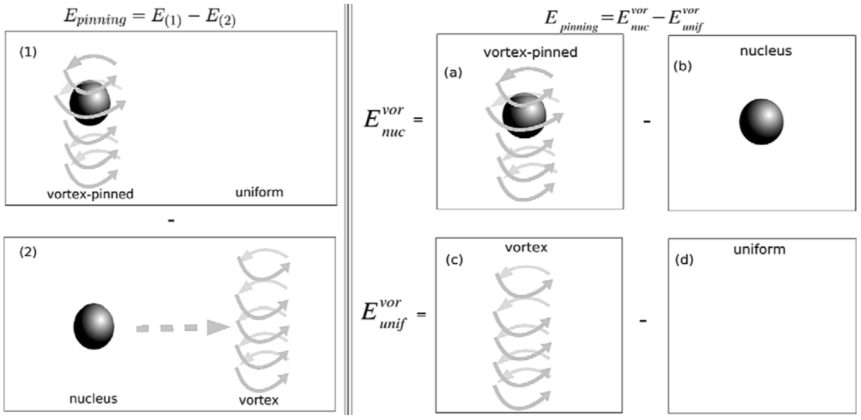

Figure 2.2: Visual representation of (2.58). This figure was taken from (Avogadro et al., 2008).

We reiterate that each calculation is performed within a box with the same dimensions (h_{box}, ρ_{box}) and with the same neutron chemical potential, so that the asymptotic density of the neutron sea is the same.

We define the binding energy of the vortex onto the nucleus as the energy to move vortex from its site on top of the nucleus to an infinite distance from it. A negative value means that the favourable position for the vortex is on top of the nucleus, whilst a positive value means that the favourable position is far away from it. An explicit expression for the binding energy can be found by subtracting the energy of a vortex pinned on a nucleus surrounded by an infinite neutron-sea (NP and NS configurations) and the energy of a vortex and a nucleus far apart in the same neutron sea (IP and Nu configurations). Practically, these two systems are obtained putting next to each other to cylindrical boxes, within which we solved the HFB equations in the specified configuration. Finally, a simple combination of the total energies gives the final expression

$$E_b = E^{NP} + E^{NS} - (E^{IP} + E^{Nu}) = E^{NP} - E^{Nu} - (E^{IP} - E^{NS}) \quad (2.57)$$

where E^i is the total energy of the i configuration. A visual representation of (2.57) is shown in Figure 2.2.

There is an extra term we must consider in (2.57), since the presence of the vortex reduces the number of neutrons found in each cell. Hence we must adjust the binding energy to account for such difference in the following way

$$E_b = E^{NP} - E^{Nu} - (E^{IP} - E^{NS}) + \lambda_n(N^{Nu} - N^{NP} - (N^{NS} - N^{IP})) \quad (2.58)$$

where N^i is the number of neutrons. This correction originates from the fact that we work within the boundaries of a finite cylindrical cell.

The reason why the binding energy does not coincide with the pinning energy lies in the fact the dimension of the Wigner-Seitz cells shrinks considerably as the density grows. As explained in Section 1.3, we need to know the value of the pinning energy at separation distance $\rho = R_{WS}$. As a consequence, the radius of the cylindrical box should be $\rho_{box} = R_{WS}/2$, so that each calculation

is contained inside the boundaries of the WS cell. In particular, when the vortex is not pinned on the nucleus, the distance between the two is exactly R_{WS}. This way, since we work in the WS approximation, we could neglect other nuclei and reasonably expect $E_p \sim E_b$.

Unfortunately, the binding energy exhibits an unphysical dependence on the radius of the box, which disappears once ρ_{box} is big enough (usually $\rho_{box} \gtrsim 35$ fm; see Appendix A). As we see from Table 1.2, the value of $R_{WS}/2$ becomes quite small. For almost any density, the binding energy does not converge yet at its asymptotic value for $\rho = R_{WS}/2$. We should then take in account the effect of neighbouring nuclei, which we are unable to do. In Figure 2.3 we show a graphic explanation of this problem.

Nevertheless, we can give an estimate for the pinning energy E_p from the binding energy E_b. If we assume that the nuclear interaction between vortex and nucleus is short ranged, then after a certain distance ρ^* such interaction will become negligible. Therefore also its contribution to the pinning energy would be negligible after ρ^*. As pointed out by Epstein and Baym in their already cited work, (Epstein and Baym, 1988), there is a kinetic component to the pinning energy, originated by the fact that the nucleus is influenced by the velocity field of the vortex. This term depends directly on the distance ρ and its explicit form is

$$K_n(\rho) = \frac{3}{2} M_s \left(\frac{\zeta - 1}{\zeta + 2}\right) \left(\frac{\hbar}{2 m_0 \rho}\right)^2 \tag{2.59}$$

where m_0 is the nucleon mass, M_s is the mass of the neutron superfluid of density n_∞ displaced by a nucleus of radius R_n

$$M_s = \frac{4}{3} \pi R_n^3 n_\infty$$

and ζ is the ratio of the nucleus density n_n to the neutron superfluid density

$$\zeta = \frac{n_n}{n_\infty}$$

K_n is always repulsive and it is inversely proportional to the square of the distance ρ between nucleus and vortex; it's expected to give a little contribution to the pinning energy at R_{WS}.

As said before, ρ^* is the distance at which the nuclear interaction between nucleus and vortex becomes negligible. We can estimate such distance as the sum of the nuclear radius R_n and the coherence length ξ of the vortex

$$\rho^* \sim R_n + \xi \tag{2.60}$$

where the explicit form of ξ is

$$\xi = \frac{\hbar^2 k_F}{\pi m_0 \Delta}$$

where k_F is the Fermi momentum. If one takes Δ as the mean of the pairing field of the neutron sea, one finds that ξ ranges from 3-4 to 10 fm approximately.

Let's suppose $\rho^* < R_{WS}$. Then at $\rho = R_{WS}$ the residual interaction between nucleus and vortex is only kinetic, so that we can write the pinning energy at separation distance R_{WS} $E_p(R_{WS})$ as

$$E_p(R_{WS}) \simeq E_b - K_n(R_{WS}) \tag{2.61}$$

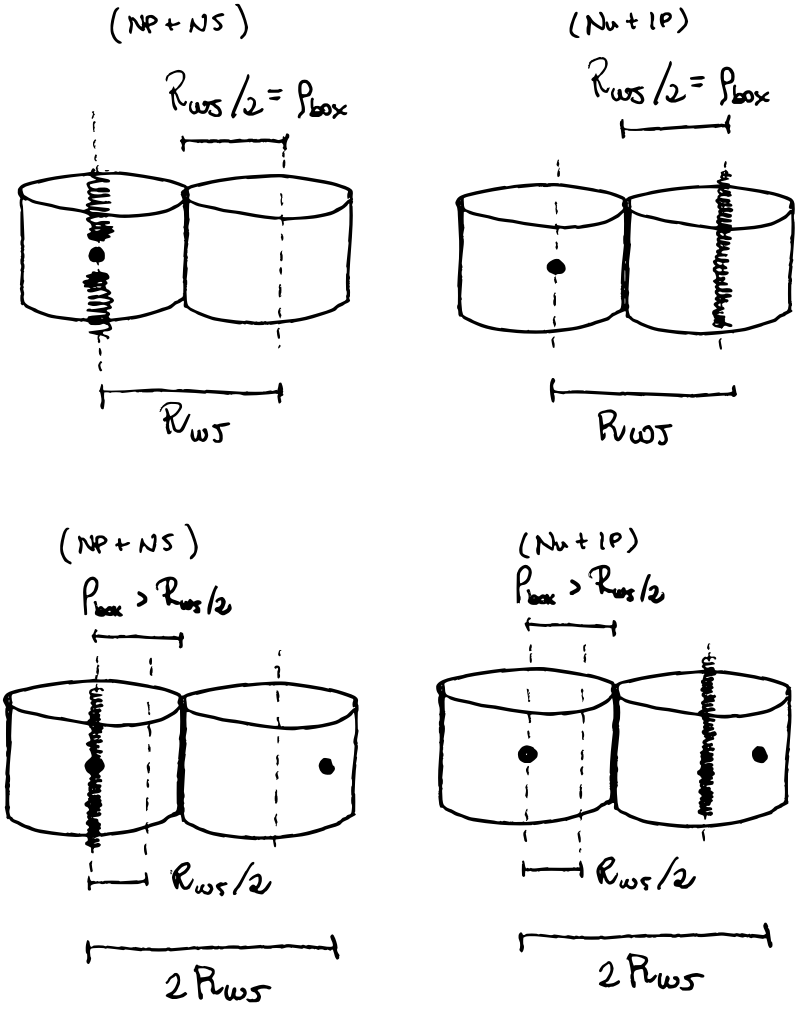

Figure 2.3: A graphic explanation of the problem regarding the binding energy. In the upper figure we show a calculation with $\rho_{box} = R_{WS}/2$. In this situation, the binding energy would coincide with the pinning energy, as the influence of neighbouring nuclei can be neglected in the WS approximation. On the contrary, this does not hold true for the lower figure, where $\rho_{box} > R_{WS}/2$. In this case, in the second box we would need to take into account the other nucleus in the lattice.

If $E_b < 0$, then the pinning energy would be slightly bigger then the binding energy, whereas if $E_b > 0$ the pinning energy would be slightly smaller then the binding energy. In either case, the sign of E_b and E_p would be the same. At R_{WS}, the contribution of $K_n(R_{WS})$ is of the order of few tens of keV. In Figure 2.4 we show a useful drawing to understand (2.61).

If, on the other hand, $\rho^* \gtrsim R_{WS}$, then the nucleus-vortex system would trespass on neighbouring WS cells; the results of our calculations could not help us in estimating the pinning energy, since we neglect the presence of the nuclear lattice.

It is important to stress that relation (2.61) holds only if the nuclear interaction between nucleus and vortex is negligible after ρ^*. We find this assumption reasonable, since nuclear interactions have short range: at distances greater than ρ^*, the overlap between nucleus and vortex is negligible.

2.6 Changes to the original code

As mentioned already, the code we used in this work was firstly employed in (Avogadro et al., 2008). We will now discuss the modification we made and in which way the results have changed.

In the original program, the proton density was forced to be spherically symmetric. This was achieved by taking spherical averages of the cylindrical neutron densities to compute the proton potential (2.38) at each step of the iterative process.The reasoning behind this choice was that that protons are deeply bound and one does not expect them to be much affected by the neutron density deviation from sphericity.

We decided to remove this constraint. The algorithm is now fully self-consistent and we can now explore the effect of the vortex on the shape of the proton density in the nucleus.

We also improved some numerical aspects of the code, namely derivatives and integrals. For the first we use a nine points formula, replacing the two points one used before. In Figure 2.5 we show the two methods at work with a trial function $f(x) = \sin(x)$. Even though the difference is small (the relative difference is approximately 3 %), the nine points formula is visibly more accurate. For the second we implemented a multi-dimensional Simpson method in place of trapezoid method used before. The relative difference between the two algorithms is approximately 1 %.

Improving the numerical precision is crucial: to compute the binding energy (3.2), we must subtract number in the order of hundreds or even thousands of MeV to find a result in the order of some MeV.

Lastly, it is important to discuss a test we did on a closed shell nucleus, ^{40}Ca.

2.6.1 ^{40}Ca simulations

In this test, we want both to verify that the code still solves correctly the HFB equations and to examine the upgrades we implemented. We apply our HFB program to the case of the atomic nucleus ^{40}Ca. This is a closed shell nucleus, both in protons and neutrons. In this case the HFB problem reduces to a spherical HF problem and we can compare our solution obtained expanding on

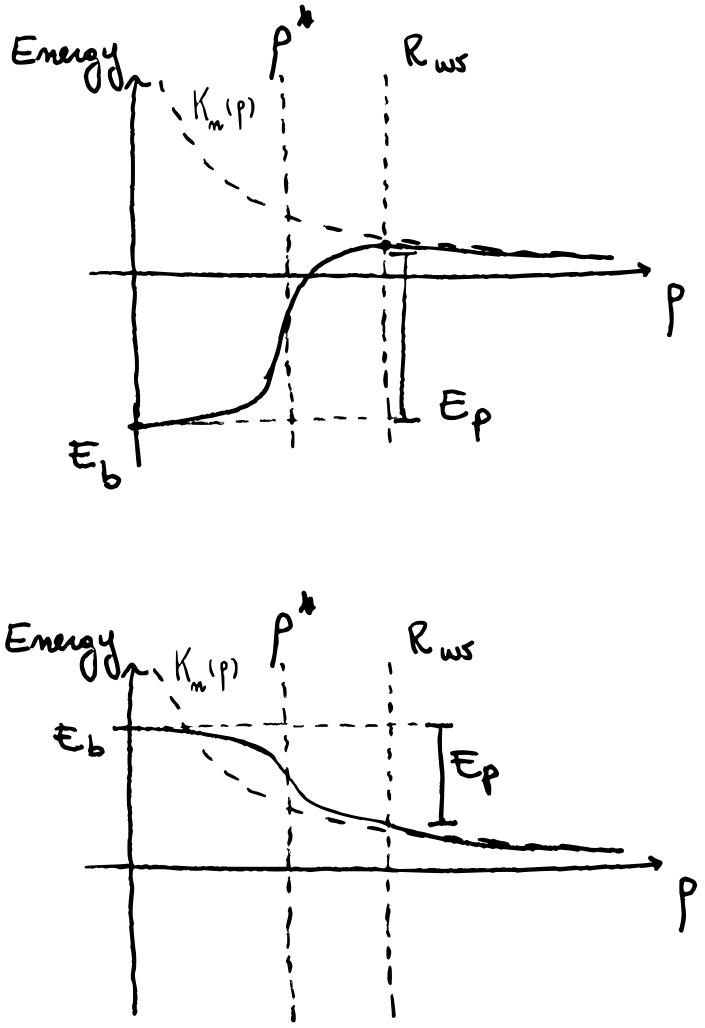

Figure 2.4: We draw an energy curve that connects the binding energy E_b, marked at $\rho = 0$ with the kinetic contribution $K_n(\rho)$ (2.59) at large ρ distances. While we cannot know the exact expression of the curve, we expect it to have a sudden drop once $\rho > \rho^*$;it then tends to $K_n(\rho)$. As we see from the figure, whether $E_b \lesseqgtr 0$, we must subtract the residual kinetic contribution $K_n(R_{WS})$ to the binding energy to obtain an estimate of the pinning energy.

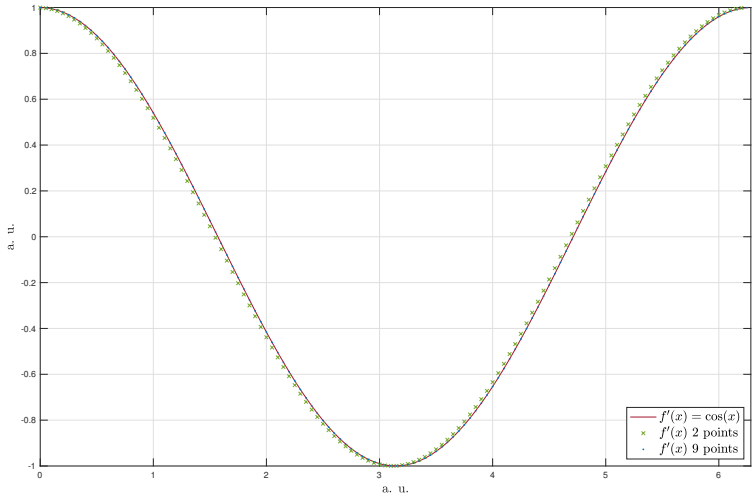

Figure 2.5: Comparison between the 9 points and 2 points derivative. We used as trial function $f(x) = \sin(x)$, so that $f'(x) = cos(x)$.

the cylindrical basis to the outcome of a HF spherical code. We use the hfrpa code of (Colò and Roca-Maza, 2021).

We use the SLy4 interaction without the spin-orbit terms. Since in the original program the Coulomb exchange potential was not implemented, it has been set to zero in the modified program and hfrpa code as well.

We focus mainly on two outputs: the total energy and the single particle levels. In Table 2.1 we show the total energy, divided among its contributions, as listed in (2.42); the only exception being E_{12}, which is defined as $E_{12} = E_{fin} + E_{eff}$. We report also the relative difference between the hfrpa results and our program.

In Table 2.2 we list the single particle energy levels of neutrons and protons. Levels with the same values of the angular momentum l are degenerate. However, the energies of the original program deviate from the exact ones by almost 1 MeV. In the neutron case, the original program produces single particle energies which are not degenerate by several hundreds of keVs. The new program instead produces both neutron and proton levels which deviate from the exact values by less than 10 keV.

	hfrpa	Original program		Modified program	
		Value	$\delta E(\%)$	Value	$\delta E(\%)$
K	640.21	653.91	2.1	638.93	0.1
E_0	−3716.80	−3721.57	0.1	−3707.01	0.3
E_3	2398.00	2394.48	0.1	−2391.19	0.3
E_{12}	279.59	280.48	0.3	278.83	0.3
E_C	78.94	77.96	1.2	78.72	0.3
E_{tot}	−320.03	−314.72	1.6	−319.33	0.2

Table 2.1: All contributions to the total energy (E_{tot}). Values are expressed in MeV. δE is the relative energy difference (in percentage) between each value and the standard HF equivalent. We divided the energy in its main contributions, as in (2.42), except for E_{12}, which is defined as $E_{12} = E_{fin} + E_{eff}$. The interaction used was SLy4 and the spin-orbit terms were neglected, as well as the Coulomb exchange potential.

Neutrons				
		hfrpa	Original program	Modified program
1s	$l_z = 0$	−47.82	−47.88	−47.799
1p	$l_z = 1$	−33.21	−33.66	−33.184
	$l_z = 0$	−33.21	−33.74	−33.182
	$l_z = -1$	−33.21	−33.66	−33.184
1d	$l_z = 2$	−18.85	−19.61	−18.785
	$l_z = 1$	−18.85	−19.80	−18.786
	$l_z = 0$	−18.85	−19.61	−18.789
	$l_z = -1$	−18.85	−19.80	−18.786
	$l_z = -2$	−18.85	−19.61	−18.785
2s	$l_z = 0$	−16.95	−17.63	−16.889
Protons				
		hfrpa	Original program	Modified program
1s	$l_z = 0$	−39.36	−39.69	−39.356
1p	$l_z = 1$	−25.29	−25.96	−25.282
	$l_z = 0$	−25.29	−25.96	−25.277
	$l_z = -1$	−25.29	−25.96	−25.282
1d	$l_z = 2$	−11.40	−12.37	−11.361
	$l_z = 1$	−11.40	−12.37	−11.362
	$l_z = 0$	−11.40	−12.37	−11.371
	$l_z = -1$	−11.40	−12.37	−11.362
	$l_z = -2$	−11.40	−12.37	−11.361
2s	$l_z = 0$	−9.48	−10.63	−9.459

Table 2.2: Energies of each single particle levels, both for protons and neutrons, expressed in MeV.

Chapter 3

Results

We will now present our results. We performed calculations for eight different neutron sea densities n_∞, spanning from $n_\infty = 0.001$ fm^{-3} to $n_\infty = 0.038$ fm^{-3}. These are the same densities studied in (Avogadro et al., 2008), so that a direct comparison between our results and theirs is straightforward.

For each density, we repeated the computation three times, varying the cylindrical box radius ρ_{box}, to ascertain that the results did not depend on it. The three values are: $\rho_{box} = 38$ fm, $\rho_{box} = 40$ fm and $\rho_{box} = 42$ fm; as for the box height, it is always set to 40 fm. We used two different Skyrme-like interactions: SLy4 and SkM* (Chabanat et al., 1997), (Bartel et al., 1982). The results will show marked dependence on the interaction. In particular, the pairing field Δ is deeply affected by this choice. In Figure 3.1 we show the pairing gap of the uniform neutron sea as a function its density n_∞; we highlighted the eight densities that were used in our calculations.

It is important to remember that, as explained in Chapter 2, we solved the HFB equations in four different configurations, each described by the presence (or absence) of a nucleus and/or a vortex. The nucleus is characterized by the proton number Z, while the vortex is defined by ν, the units of angular momentum carried by it. We explored only $\nu = 1$, since it is a commonly accepted fact that superfluid vortexes tend not to have $\nu > 1$. As for the nucleus, we always set $Z = 40$, because, if one neglects the spin-orbit interaction, it is at shell closure (Negele and Vautherin, 1973).

So, the four configurations of our computations are: neutron sea (NS, $Z = 0$, $\nu = 0$); nucleus in the sea (Nu, $Z = 40$, $\nu = 0$); vortex in the neutron sea, or interstitial pinning (IP, $Z = 0$, $\nu = 1$); vortex on top of a nucleus, or nuclear pinning (NP, $Z = 40$, $\nu = 1$).

We will begin showing figures of the key quantities (density, pairing gap and self-potential) for the different configurations, highlighting the differences arising from growing external neutron-sea density and from using different interactions.

We will continue our discussion of the results focusing on the effects of the vortex on the proton density and assess if there is any deformation. We will then conclude our analysis giving estimates for the pinning energies and comparing them to the results of the already cited works.

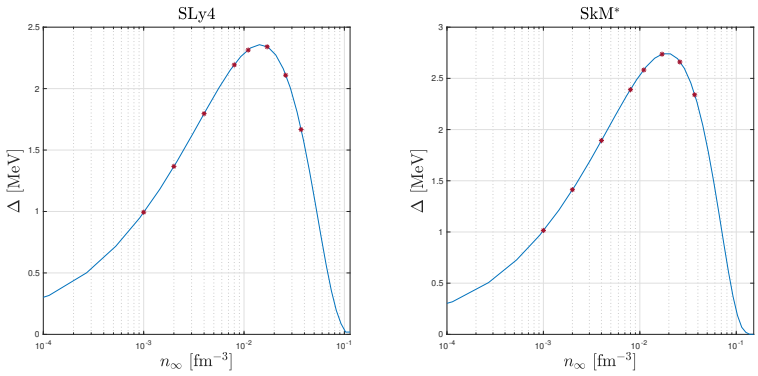

Figure 3.1: Pairing gap as a function of the uniform neutron sea density. We highlighted the value of Δ for the eight different densities we work with. On the left we used the SLy4 interaction, while on the right SkM*.

3.1 Nucleus in the sea ($Z = 40$, $\nu = 0$)

We show in Figure 3.2 the densities and self-potentials of neutrons and protons for the SLy4 interaction, for $n_\infty = 0.004$ fm^{-3}. Spherical symmetry is maintained, as one would expect from a closed shell nucleus in uniform neutron matter. In fact, as we can see, the dependence along the ρ and z axis is practically the same.

As for the neutron density, it follows a Wood-Saxon like function in the proximity of the nucleus, while far away is constant. Writing it explicitly, one has

$$f(r) = n_\infty + \frac{n_0}{1 + \exp\left(\frac{r - R_n}{a_0}\right)} \tag{3.1}$$

where $r = \sqrt{\rho^2 + z^2}$, n_0 is a density parameter, R_n is the radius of the nucleus and a_0 is the diffusivity.

In Figure 3.3 we compare the densities with the function f. From the various cuts at different z values, we can see that the densities can be appropriately fit with a function that depends only on the distance from the center of the nucleus.

As for the self-consistent potentials, we show them in Figure 3.4 for three different neutron sea densities. They are quite deep, although the SLy4 interaction potential is deeper. Like the density, they present a spherical symmetry.

Lastly, let's focus on the neutron pairing gap Δ, shown in Figure 3.5 for both interactions: SLy4 is on the left, while SkM* is on the right. As we have showed, in the Nu configurations the quantities are approximately spherical, so that we chose to show our result only for $z = 0$ plane.

Since the pairing gap is a very delicate quantity and since it affects deeply the results of our work, we have decided to plot it for four different surrounding densities. The first observation is that, within the nucleus radius, Δ is only a fraction of its asymptotic value. This is not unexpected: from eq. (2.43) and Figure 2.1, we see that the closer the density is to the nuclear saturation density, the more the pairing is suppressed. Far from the nucleus, instead, Δ reaches the same value of the neutron sea, as shown in Figure 3.1.

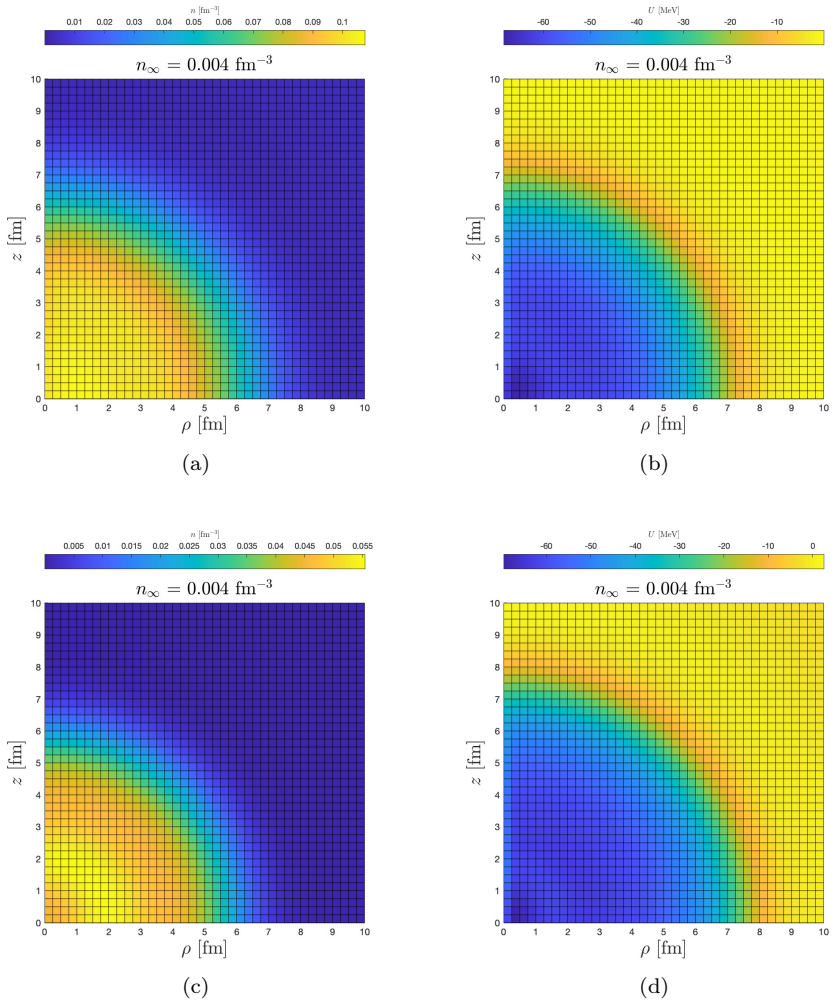

Figure 3.2: Neutron density and self-consistent potential (top) and proton density and self-consistent potential (bottom). The surrounding neutron sea density is $n_\infty = 0.004$ fm^{-3} and the interaction used is SLy4.

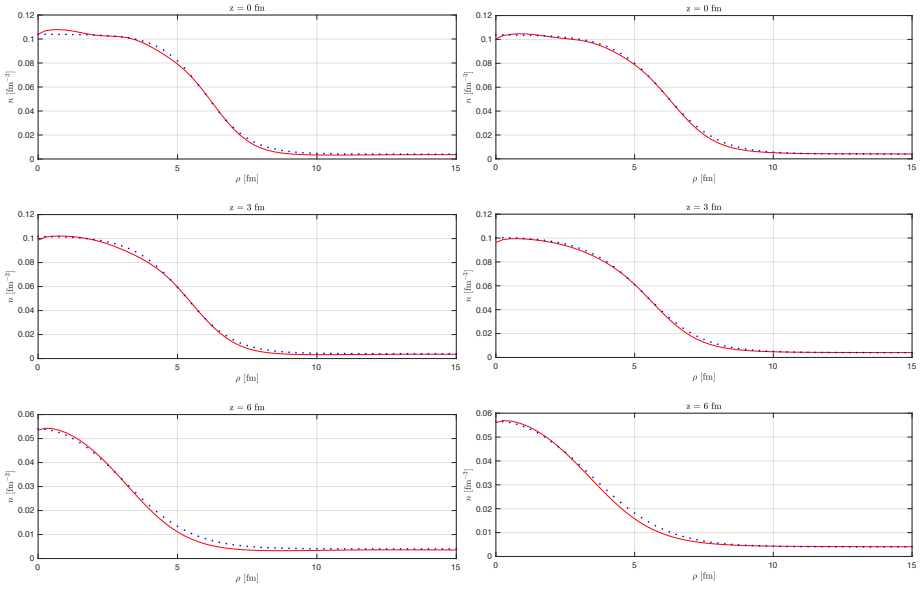

(a) (b)

Figure 3.3: Neutron density (red full line) in comparison with (3.1) (blue dotted points), shown for several cuts perpendicular to the z-axis, taken at different values of z. On the left there is SLy4, and the parameters are: $R_n = 6.0$ fm, while $a_0 = 0.8$ fm and $n_0 = 0.1$ fm^{-3}. On the right there is SkM*, and the parameters are: $R_n = 6.1$ fm, while $a_0 = 0.95$ fm and $n_0 = 0.1$ fm^{-3}. The diffusivity parameters a_0 are greater than the usual nuclear value $a_0 \sim 0.6$ fm. The surrounding neutron sea density is $n_\infty = 0.004$ fm^{-3}.

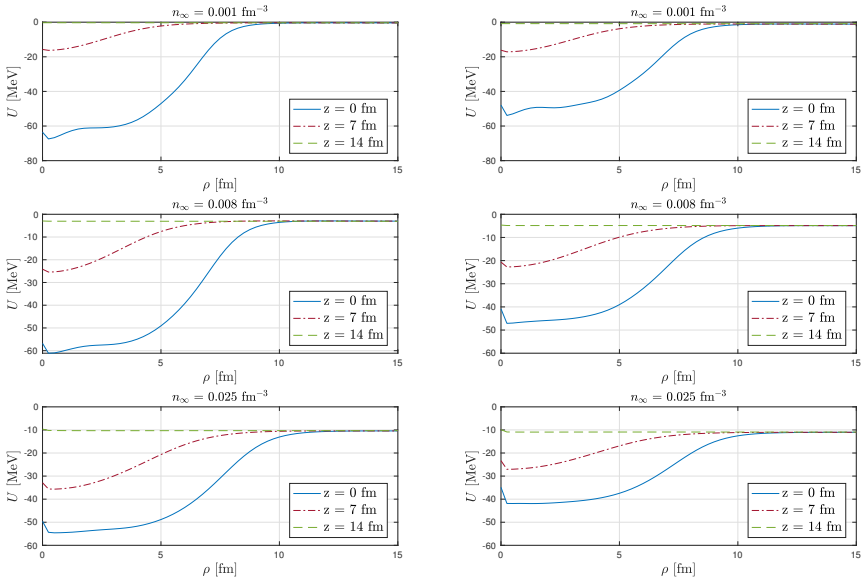

(a) (b)

Figure 3.4: Neutron self-consistent potentials for three different values of the surrounding density. On the left there is SLy4, while on the right SkM*.

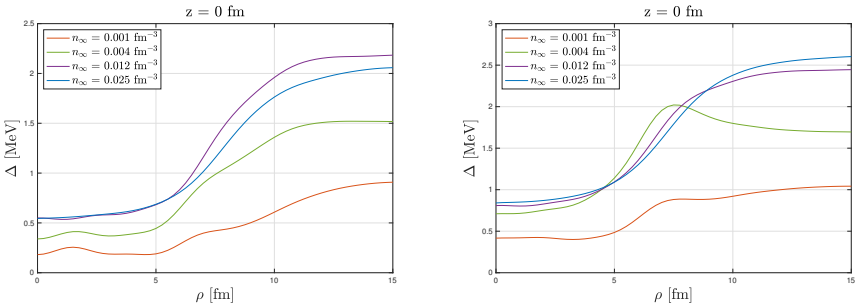

(a) (b)

Figure 3.5: Neutron pairing gaps for four different neutron sea densities. On the left there is SLy4, on the right is SkM*. The suppression of the gap is due to the high densities inside the nucleus. At large distances Δ reaches the asymptotic value. Δ is clearly dependent on both the interaction chosen and the external neutron sea density value.

Secondly, one can appreciate qualitatively different behaviour for different surrounding densities, opposed to the previous discussed quantities.

Finally, it is important to acknowledge that the interaction plays an important role. SLy4 produces lower pairing gaps than SkM* and the curves are qualitatively different as well. In fact, SLy4 rises to its asymptotic value more slowly than SkM*.

3.2 Vortex in the sea ($Z = 0$, $\nu = 1$)

The solutions of the HFB equations for neutron matter threaded by a vortex give a suppression of the density and the pairing gap close to the vortex axis region, as we show in Figure 3.6.

The pairing gap at $\rho = 0$ vanishes; it rises linearly at small distances and more slowly once it is approaching its asymptotic value. The neutron density has an analogous behaviour, with the exception that at $\rho = 0$ it is approximately half of the asymptotic neutron sea value. The impact of different interactions is not very relevant for these quantities. Our results are similar to those presented in (Yu and Bulgac, 2003), where the authors studied an isolated vortex in uniform neutron matter.

It is also interesting to show the velocity field of the neutrons. We show our results in Figure 3.7 at $z = 0$ fm.

Negative values mean that the superfluid flows clockwise. At large distances, the velocity field tends to its expected behaviour $\frac{\hbar}{2m_n\rho}$, whilst it vanishes approaching the vortex core, where the neutrons are not superfluid anymore.

We can understand why superfluidity vanishes in a region close to the rotation axis in the following way.

A superfluid condensate forms because it lowers the total energy of the system. If there is a vortex in such condensate, particles pairs carry one unit of angular momentum, since $\nu = 1$. Classically, this means that the closer to the vortex axis the greater the velocity and, directly, the greater the kinetic energy.

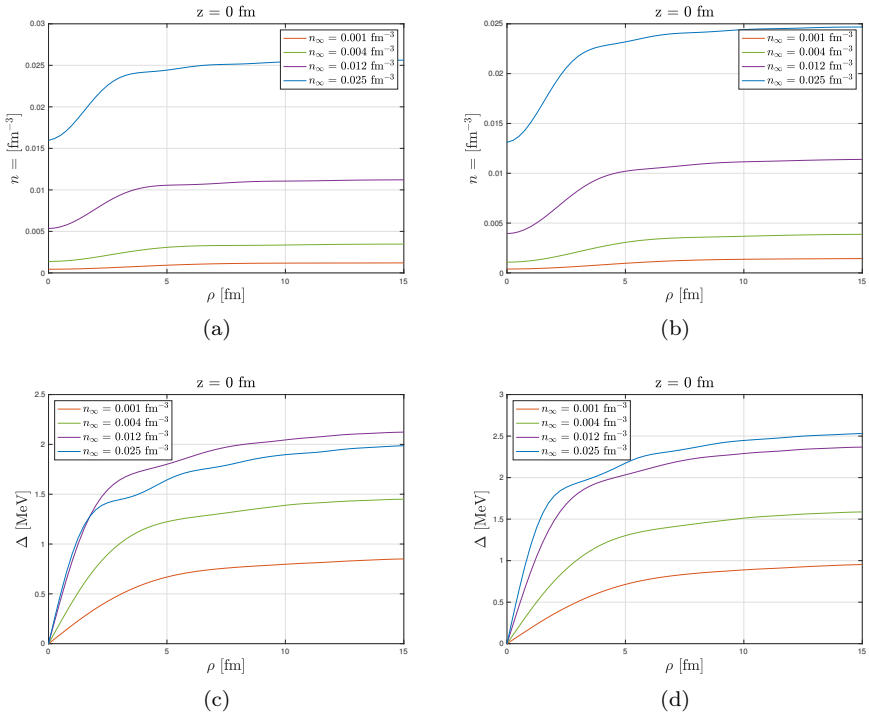

Figure 3.6: Density (top) and pairing gap (bottom) of neutron matter threaded by a vortex. On the left there is SLy4, on the right SkM*. We investigated four different densities. All the quantities shown present a suppression near the center of the vortex.

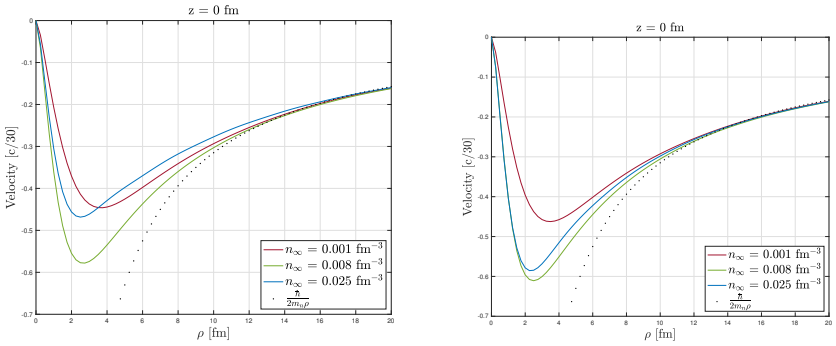

(a) (b)

Figure 3.7: Velocity field of a vortex in a neutron sea for SLy4 (left) and SkM* (right), for three different densities. Far from the vortex core, where the neutrons become again superfluid, the velocity assumes the expected behaviour $\frac{\hbar}{2m_n\rho}$.

Eventually, the gain in kinetic energy will outweigh the energy reduction due to pairing. Hence, the superfluid condensate will be no more the optimal configuration: in the center of the vortex neutron matter is no more superfluid and there is no vortical flow.

3.3 Vortex on a nucleus ($Z = 40$, $\nu = 1$)

Let's focus on the pairing fields. In Figure 3.8, we show the gaps for the two interactions (SLy4 top, SkM* bottom), at different z values and for four surrounding densities.

For almost all cases, the pairing fields are suppressed in the nuclear region and along the z axis as well. On the contrary, for $n_\infty = 0.025$ fm^{-3} the pairing gap calculated with SkM* survives in the nuclear interior, indicating that the vortex actually penetrates the nucleus at high density with the SkM* interaction.

Furthermore, in the upper part of Figure 3.9, we compare the pairing gaps of the four different configurations for the SLy4 interaction, at $n_\infty = 0.004$ fm^{-3}. We translated by 7 fm the pairing gap of IP configuration, to show that, outside the nuclear region, the vortex pinned onto a nucleus behaves similarly to a vortex in uniform neutron matter. On the other hand, we see that the pairing gap of the nucleus rises in a different way. In other words, the vortex is expelled from the nucleus and encircles it.

As for SkM* (lower part of Figure 3.9), it is more instructive to plot only the NP and IP configuration for only two neutron sea densities, $n_\infty = 0.001$ fm^{-3} and $n_\infty = 0.025$ fm^{-3}. For the lower density, the behaviour is quite similar to the one we observe with SLy4. This is no surprise, since the pairing gaps are similar. For the higher density, Δ rises slower in the NP configuration, meaning that we cannot give the same interpretation.

We now show the velocity field of the vortex pinned in Figure 3.10 at three different values of z: 0, 7 and 14 fm. For SLy4 (up), only $n_\infty = 0.004$ fm^{-3} is plotted, while for SkM* (down) $n_\infty = 0.001$ fm^{-3} and $n_\infty = 0.025$ fm^{-3} are plotted instead. For all but the latter density, we observe a suppression of the

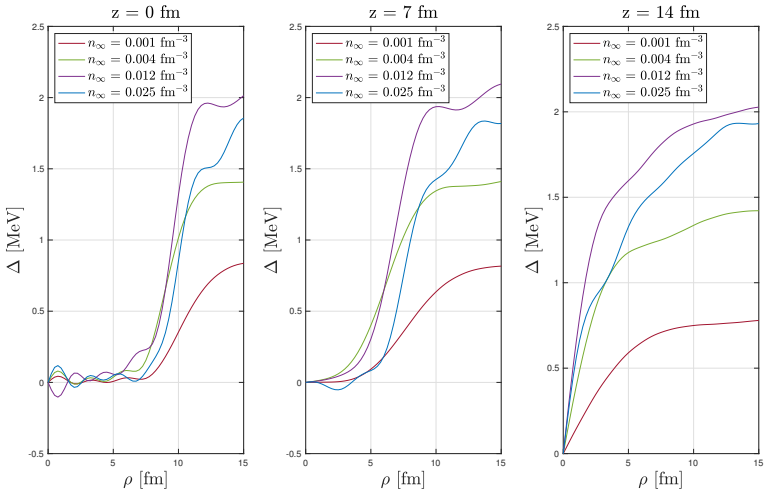

(a)

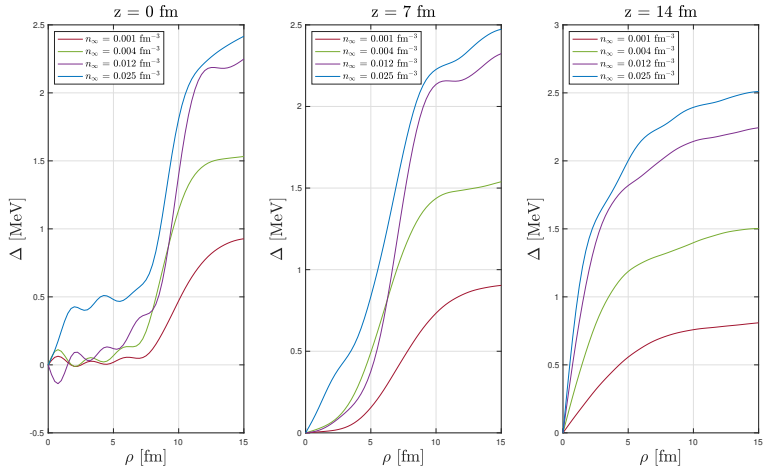

(b)

Figure 3.8: Pairing gap of a vortex on top of a nucleus, surrounded by a neutron sea at various densities, for three different values of z. In the top figure there is SLy4, in the bottom one SkM*. The pairing is suppressed inside the nuclear region and along the z axis; outside it grows first linearly and then more slowly once it's approaching the asymptotic value. On the other hand, for $n_\infty = 0.025$ fm^{-3} with SkM*, there is a non zero field inside the nucleus. Outside the boundaries of the nuclear region, ($z = 14$ fm), the pairing gap behaves as in neutron matter Figure 3.6.

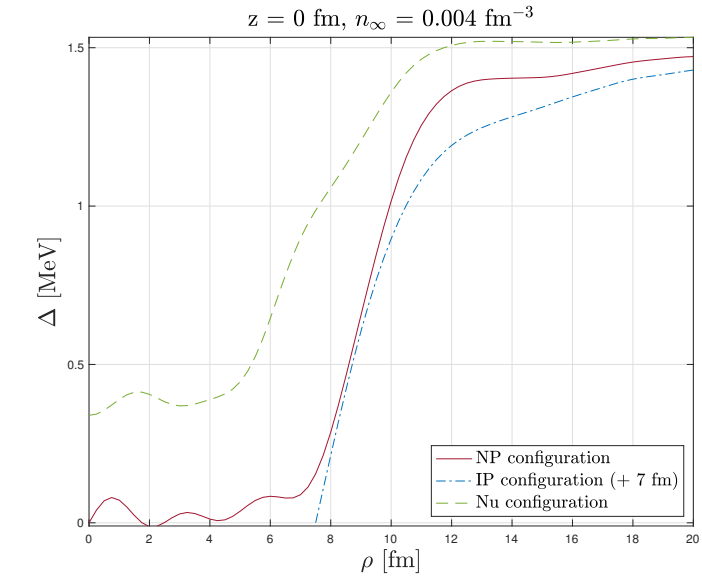

(a)

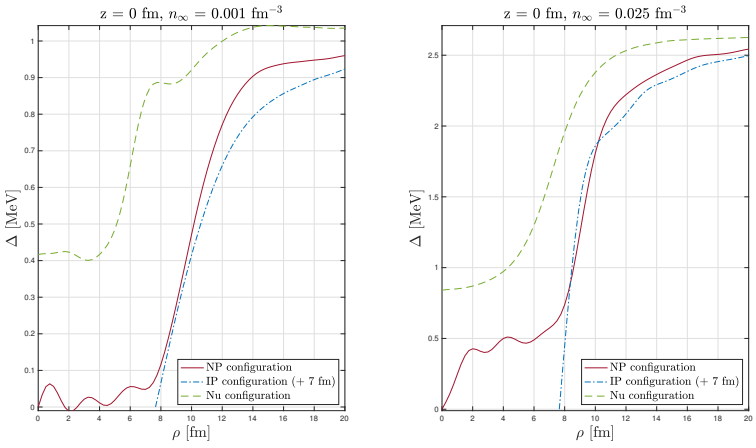

(b)

Figure 3.9: Pairing gap of the different configurations, at $z = 0$ for SLy4 (top) and SkM* (bottom). Since for SLy4 there is no behaviour difference between different surrounding densities, we plotted only $n_\infty = 0.004$ fm^{-3}. For SkM*, we instead plotted at $n_\infty = 0.001$ fm^{-3} and at $n_\infty = 0.025$ fm^{-3} and only the NP and IP configurations. The IP pairing gap is translated by 7 fm, to highlight the fact that it rises in a similar way to the NP configuration outside the nuclear region. For SkM*, for $n_\infty = 0.025$ fm^{-3}, the gap rises more slowly compared to vortex growth.

velocity field in the nuclear region, hence confirming our hypothesis that the vortex cannot penetrate the nucleus and instead encircles it. On the other hand, for $n_\infty = 0.025$ fm^{-3} with SkM*, there appear to be some residual velocity inside the nucleus. The qualitative behaviour is profoundly different: at high neutron sea densities, the vortex survives inside the nucleus with SkM*.

Finally, the cut at $z = 14$ fm is almost identical to the velocity field in Figure 3.7: away from the nucleus, the vortex has the same proprieties of a vortex in neutron matter. As one would expect, all the lines connect with the asymptotic behaviour $\frac{\hbar}{2m_n\rho}$.

3.4 Vortex effects on the density

We now focus the attention on the effects of the vortex upon the neutron and proton densities. In the original code (Avogadro et al., 2008), protons were bound to have a spherical symmetry. As we have explained in the previous chapter, we have removed this constraint. It is important to see if and how much the presence of a vortex modifies the proton density in the nucleus.

First, we show in Figure 3.11 contour plots of the difference between neutron densities in the NP and Nu configuration, for two different surrounding neutron-sea densities, $n_\infty = 0.004$ fm^{-3} (3.11a SLy4 and 3.11b SkM*) and $n_\infty = 0.038$ fm^{-3} (3.11c SLy4 and 3.11d SkM*). For the lower densities, there is little to no deformation between the two configurations. Inside the innermost nuclear region ($\sqrt{\rho^2 + z^2} \lesssim 3$ fm), we can see that the difference, whether positive or negative, has a circular shape. In the outer (3 fm $\lesssim \sqrt{\rho^2 + z^2} \gtrsim 7$ fm) we see a that the NP-configuration density tends to be lower near the z axis, especially with the SLy4 interaction.

In Section 3.2 we observed that the vortex causes a density depletion near its center. We can observe such depletion just outside the nucleus and near the z axis, where the blue assumes darker tones. This is the footprint of the vortex, as it does not penetrate the nuclear region but instead encircles the nucleus.

At higher surrounding densities we can appreciate the appearance of deformed densities. For the SLy4 interaction, the neutrons in the NP configuration assume a prolate shape. On the other hand, with SkM* neutron density seem to be higher in a narrow region along the ρ axis, while to be lower almost everywhere in the vicinity of the z axis. This is peculiar of the SkM* interaction and can be interpreted as the action of the vortex penetrating into the nuclear region. As we have precedently observed, neutron matter exhibits a drop in density in the vicinity of the vortex axis.

The vortex effect is therefore more relevant the higher the surrounding neutron density is.

As for proton densities, we refer to Figure 3.12, where we show contour plots of the difference between the NP and Nu configuration, for the same two neutron-sea densities, $n_\infty = 0.004$ fm^{-3} (3.11a SLy4 and 3.11b SkM*) and $n_\infty = 0.026$ fm^{-3} (3.11c SLy4 and 3.11d SkM*).

At the lower density, SLy4 protons present almost no deformation, except for a narrow region ~ 5 fm distant from the center. The proton density is in fact suppressed near the z axis, at ~ 5 fm. This is somewhat similar to the neutron behaviour in 3.11a. The deformation is negligible for the SkM* interaction instead.

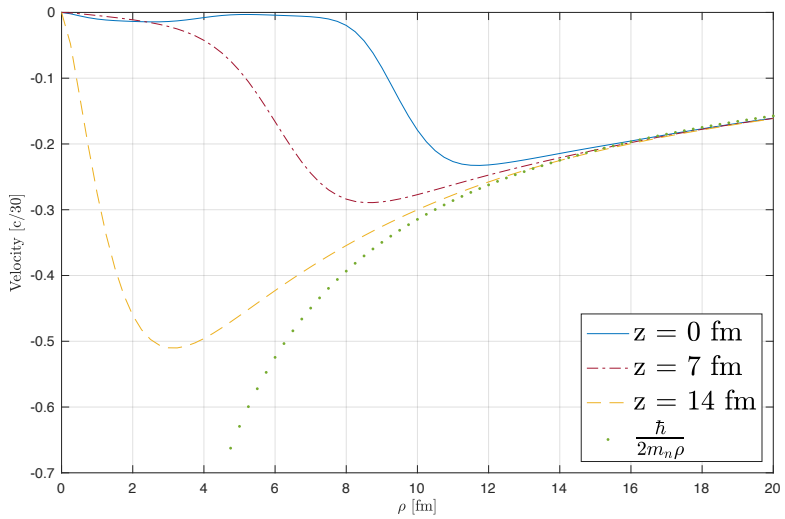

(a)

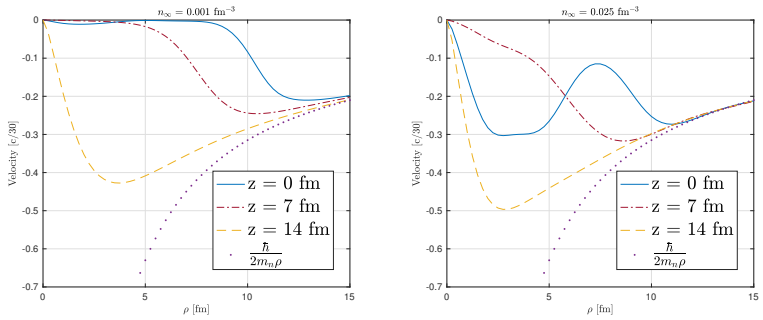

(b)

Figure 3.10: Velocity field of a vortex pinned on a nucleus in a neutron sea, for three different values of z. The surrounding neutron sea densities are $n_\infty = 0.004$ fm^{-3} for SLy4 (top), and $n_\infty = 0.001$ fm^{-3} and $n_\infty = 0.025$ fm^{-3} for SkM* (bottom). The expected behaviour $\frac{\hbar}{2m_n\rho}$ is reached away from the nucleus and from the vortex core. We notice that for SkM* the velocity field at the highest density does not vanish in the nuclear interior, contrary to the other cases.

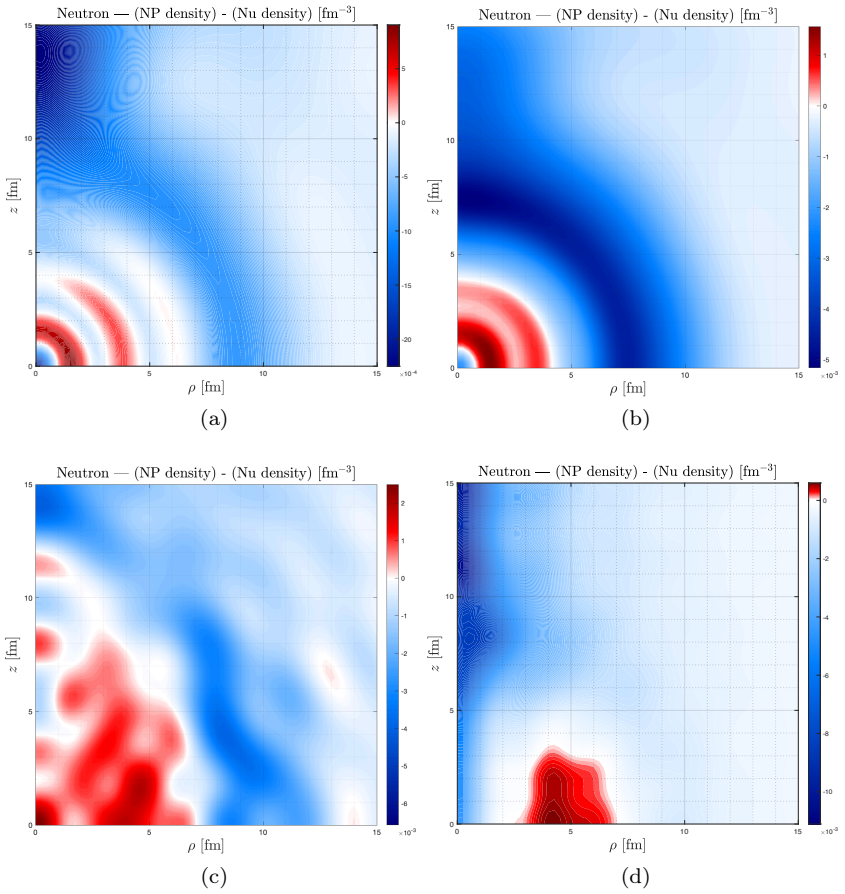

Figure 3.11: Contour plot of the difference between NP-configuration neutron density and Nu-configuration neutron density, for two neutron sea densities: $n_\infty = 0.004$ fm^{-3} (top) and $n_\infty = 0.038$ fm^{-3} (bottom). On the left there is SLy4, on the right SkM*. The positive values are colored in red, while the negative ones in blue. At lower density there is little deformation for both interactions. At higher density, neutrons assume a prolate shape with SLy4, elongating along the z axis. On the contrary, with SkM* we observe a density depletion near the z axis, due to the vortex penetrating the nuclear region.

At the higher density, for SLy4 we can observe a marked prolate shape. On the contrary, for SkM* protons seem to assumed a clear oblate shape, with an evident suppression for the higher values of z. This behaviour reflects the neutron behaviour in Figure 3.11d; it is a consequence of the vortex penetrating nuclear matter.

3.5 Pinning Energies

We now present the results for the pinning energies. As we explained in Section 2.5, the pinning energy is obtained subtracting from the binding energy E_b

$$E_b = E^{NP} - E^{Nu} - (E^{IP} - E^{NS}) + \lambda_n(N^{Nu} - N^{NP} - (N^{NS} - N^{IP})) \quad (3.2)$$

the kinetic contribution $K_n(\rho)$

$$K_n(\rho) = 2\pi n_\infty m_0 R_n^3 \left(\frac{\zeta - 1}{\zeta + 2}\right) \left(\frac{\hbar}{2m_0\rho}\right)^2 \quad (3.3)$$

evaluated at the Wigner-Seitz radius $\rho = R_{WS}$. Here, m_0 is the neutron mass, n_∞ is the external neutrons sea density, $\zeta = n_n/n_\infty$ is the ratio between the nuclear density and the surrounding density and R_n is the nuclear radius. Thus we have

$$E_p(R_{WS}) \simeq E_b - K_n(R_{WS}) \quad (3.4)$$

$K_n(R_{WS})$ is a small correction to the binding energy, its value ranging from tens of keV to few hundreds of keV; for the exact values, we remand to Appendix A. To estimate the uncertainty on the pinning energy, we follow the error propagation rule

$$\sigma_{E_p} = \sqrt{\sigma_{E_b}^2 + \sigma_{K_n}^2} \quad (3.5)$$

where σ_{E_b} is the uncertainty on the binding energy (we will explain soon how it is calculated) and σ_{K_n} is obtained from (3.3) with the error propagation formula, the errors deriving from R_n and R_{WS}.

A positive value of E_p means that the vortex is repelled by the nuclei in the lattice and it is pinned at the edge of the WS cell (interstitial pinning). A negative value, on the other hand, means that the vortex is attracted by the nucleus and it is pinned on top of it (nuclear pinning).

Lastly, before using (3.4) to compute the pinning energy, we must ascertain whether

$$\rho^* = R_n + \xi < R_{WS}$$

where R_n is the radius of the nucleus and ξ is the vortex coherence length

$$\xi = \frac{\hbar^2 k_F}{\pi m_0 \Delta}$$

where k_F is the Fermi momentum of the surrounding neutron sea. We give in Table 3.1 the results of our control.

We remind that we used the same external neutron sea densities as the ones in the original work (Avogadro et al., 2008), so that we can directly compare our results with theirs.

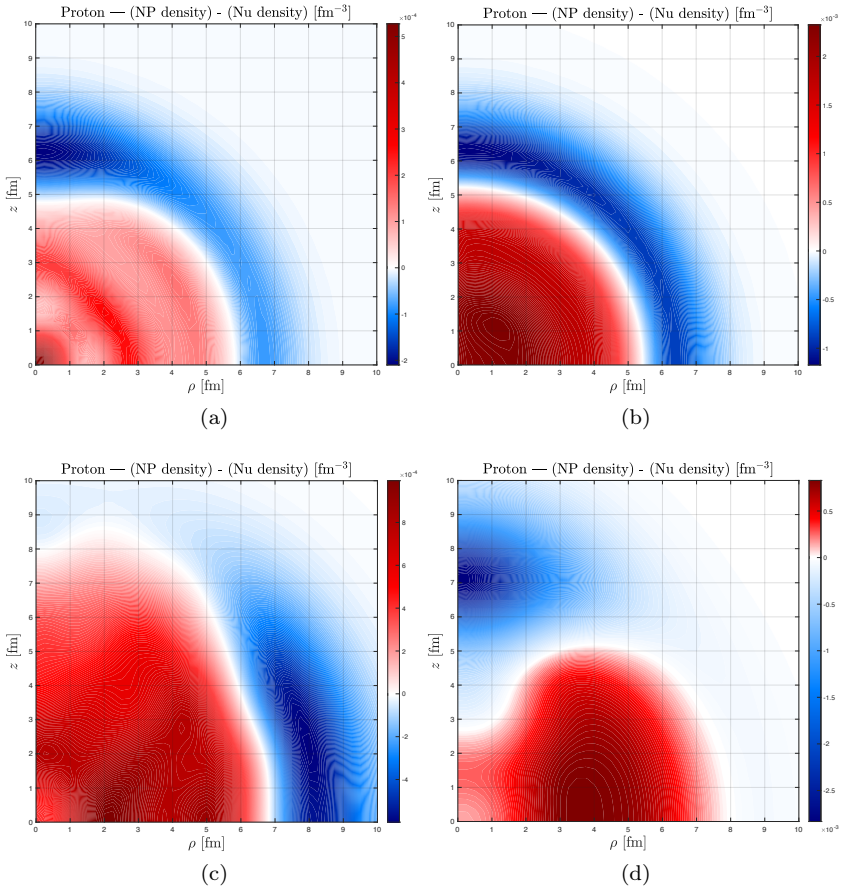

Figure 3.12: Contour plot of the difference between NP-configuration proton density and Nu-configuration proton density, for two external neutron sea densities: $n_\infty = 0.004$ fm^{-3} (top) and $n_\infty = 0.038$ fm^{-3} (bottom). On the left there is SLy4, on the right SkM*. The positive values are colored in red, while the negative ones in blue. At lower densities there is little deformation, both for SLy4 and SkM*. At higher densities protons assume with SLy4 a prolate shape in the outer region and an oblate shape in the inner regions. For SkM* there is instead a marked oblate shape.

n_∞ [fm^{-3}]	R_n [fm]	ξ [fm]	ρ^* [fm]	R_{WS} [fm]
0.001	7.31	4.56	11.88	43.7
0.002	7.29	4.32	11.62	41.5
0.004	7.24	3.98	11.21	38.8
0.008	7.13	3.95	11.09	33.7
0.011	7.03	4.13	11.17	31.8
0.017	6.93	4.62	11.55	28.9
0.026	6.73	5.75	12.49	25.6
0.037	6.57	7.98	14.55	21.4

Table 3.1: Values of ρ^* for all the density we consider, computed with the SLy4 interaction. For all densities we have $\rho^* < R_{WS}$, so that we can use (3.4) to compute the pinning energy. The results with the SkM* interaction differ slightly, and the condition $\rho^* < R_{WS}$ is always met.

For each density, we performed three calculations with a different box radius: $\rho_{box} = 38$ fm, $\rho_{box} = 40$ fm and $\rho_{box} = 42$ fm. Hence, we computed the binding energy E_b via (3.2); σ_{E_b} are computed as the root of the squared sum of the differences between each quantity appearing in (3.2) with the value of the same quantity computed in the second-last iteration. Using (3.4) and (3.5), we can estimate the pinning energies with their error.

It is crucial to control if the pinning energies have reached convergence, i.e. whether they are independent of the radius of the box. Given the fact that we estimate the pinning energy as the difference between values of order of thousands of MeV (see (3.2) and Appendix B), we say that convergence is reached if values are no more than 500 keV apart one from the other. Even though this interval is greater than all of the error bars, we must remind that σ_{E_b} can be arbitrary small given enough iterations; on the other hand σ_{K_n} is of order of few hundreds of keV at most (see Appendix B).

In Figure 3.13 we show the pinning energies for each one of our computations with the SLy4 interaction. Almost all calculation meet our criteria. For $n_\infty = 0.011$ fm^{-3} and $n_\infty = 0.037$ fm^{-3} the calculation at $\rho_{box} = 38$ fm gives a value too far from the others; it would be appropriate to control at bigger radii ($\rho_{box} = 44$ fm and maybe even $\rho_{box} = 46$ fm) whether or not the pinning energy has converged. On the other hand, for $n_\infty = 0.002$ fm^{-3} the calculation at $\rho_{box} = 40$ fm is barely acceptable and should be investigated further.

In Figure 3.13 we show the pinning energies for each one of our computations with the SkM* interaction instead. Our criteria are met in all but the higher two densities, where the calculations at $\rho_{box} = 38$ fm and $\rho_{box} = 40$ fm are not reliable. We should definitely investigate at bigger radii to control whether convergence has been reached. Nonetheless, it is not unreasonable to suppose that the results at $\rho_{box} = 42$ fm are acceptable.

We conclude our analysis showing how the pinning energy varies as a function of the external neutron sea density. We used a weighted average to combine the three pinning energies values of each surrounding density into one. For SLy4 interaction, we have ignored the result at $\rho_{box} = 38$ fm for $n_\infty = 0.011$ fm^{-3} and $n_\infty = 0.037$ fm^{-3}, as the values at $\rho_{box} = 40$ fm and $\rho_{box} = 42$ fm seem to have reached convergence.

n_∞ [fm^{-3}]	E_p [MeV]	
	SLy4	SkM*
0.001	-0.722 ± 0.003	-0.189 ± 0.007
0.002	-0.920 ± 0.004	-0.105 ± 0.007
0.004	-0.870 ± 0.003	1.59 ± 0.01
0.008	3.12 ± 0.07	7.47 ± 0.03
0.011	2.23 ± 0.20	8.10 ± 0.05
0.017	10.13 ± 0.14	11.04 ± 0.1
0.026	12.40 ± 0.21	19.79 ± 0.4
0.037	15.47 ± 0.25	24.55 ± 1.80

Table 3.2: Pinning energy for eight different values of the neutron sea density.

In Figure 3.15 and in Table 3.2 we show the the results of our analysis: we plot the pinning energy as a function of the neutron sea density. For reference, we compare it with original results of (Avogadro et al., 2008). We find moderate nuclear pinning at the lower densities (~ -1 MeV), while at higher density we find very strong interstitial pinning. Qualitatively, the pinning energy has the same trend regardless of the interaction used.

Comparing it with the original results, whilst the behaviour is similar for SkM* interaction, for SLy4 this holds true only for the first two points. After that, our calculation predicts that the pinning energy tends to grow with the surrounding density, although not monotonically increasing. On the contrary, the original SLy4 results seem to suggest that the pinning energy has an oscillatory behaviour.

All the numerical results regarding each calculation (divided into ρ_{box}, n_∞ and interaction used) are given in Appendix B.

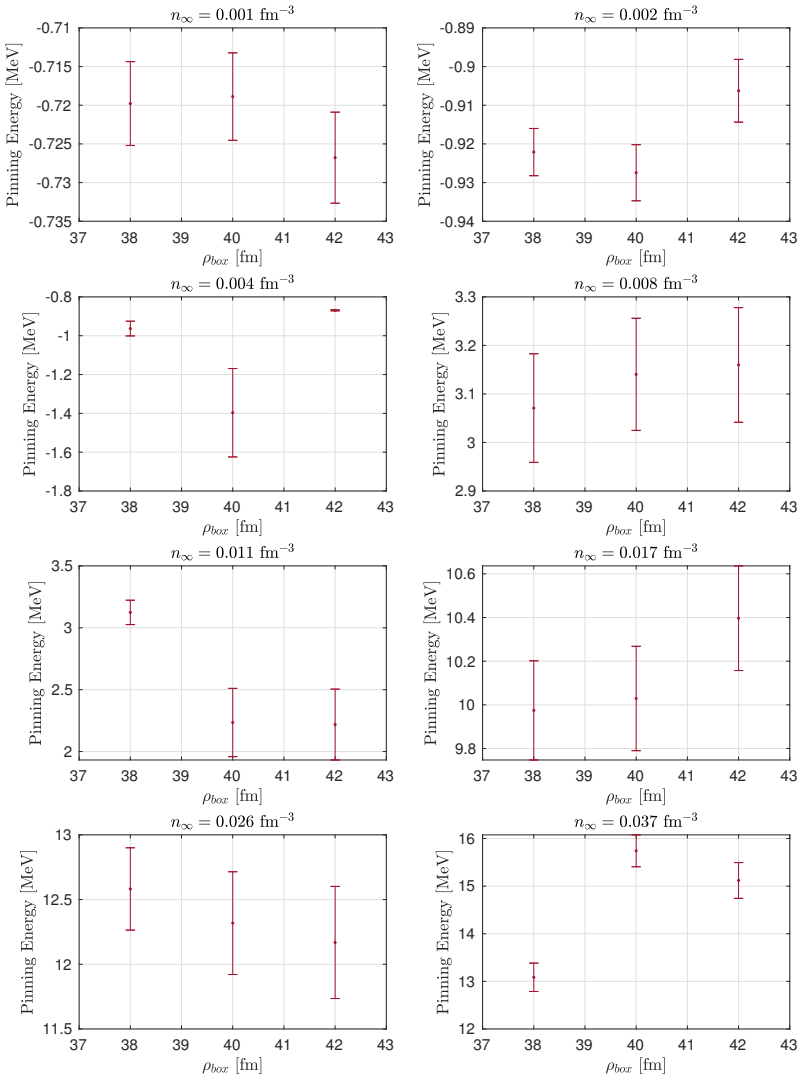

Figure 3.13: The pinning energy vs. the radius of the box, for each of the different densities, with SLy4 interaction. The error bars are the estimated numerical error on our estimate, following (3.5). Three points do not meet our criteria: $\rho_{box} = 38$ fm for $n_\infty = 0.011$ fm^{-3} and $n_\infty = 0.037$ fm^{-3} (too different from the others) and $n_\infty = 0.002$ fm^{-3} at $\rho_{box} = 40$ fm, which is barely acceptable. The interaction used is SLy4.

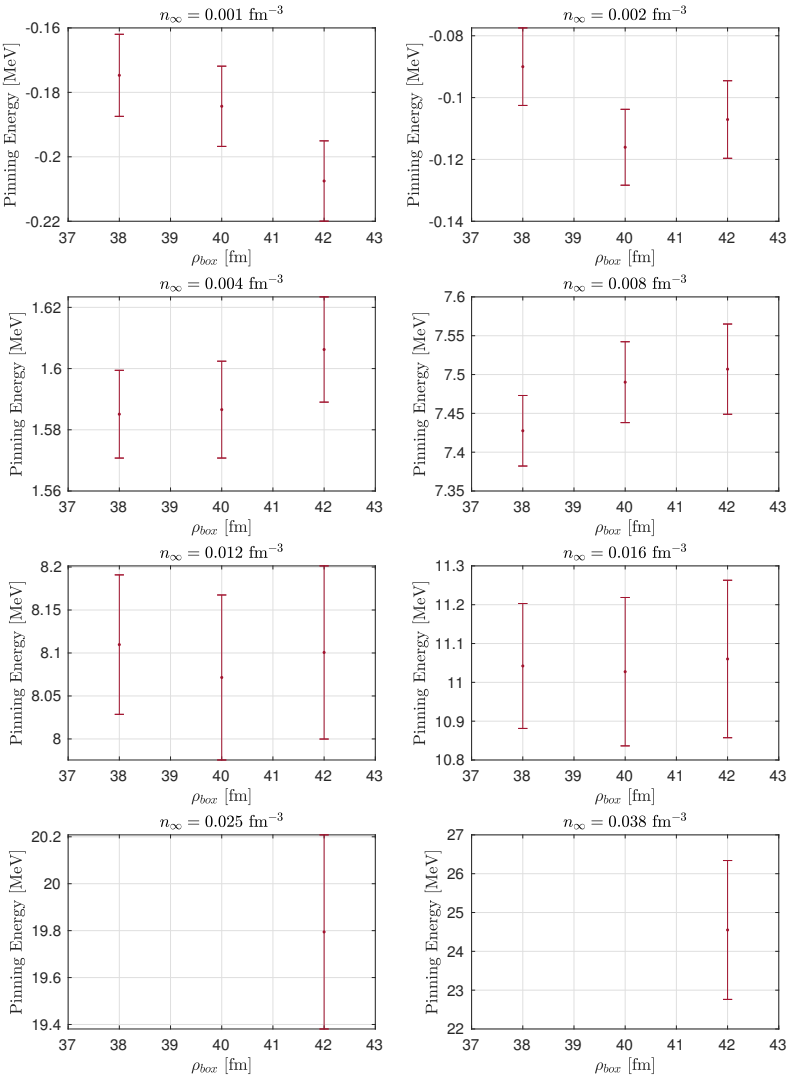

Figure 3.14: The pinning energy vs. the radius of the box, for each of the different densities, with SkM* interaction. The error bars are the estimated numerical error, following (3.5). For $n_\infty = 0.026$ fm^{-3} and $n_\infty = 0.037$ fm^{-3}, the computations where not reliable for $\rho_{box} = 38$ fm and $\rho_{box} = 40$ fm, and for $n_\infty = 0.037$ fm^{-3} also the value at $\rho_{box} = 42$ fm has a quite big uncertainty compared to all other reported values.

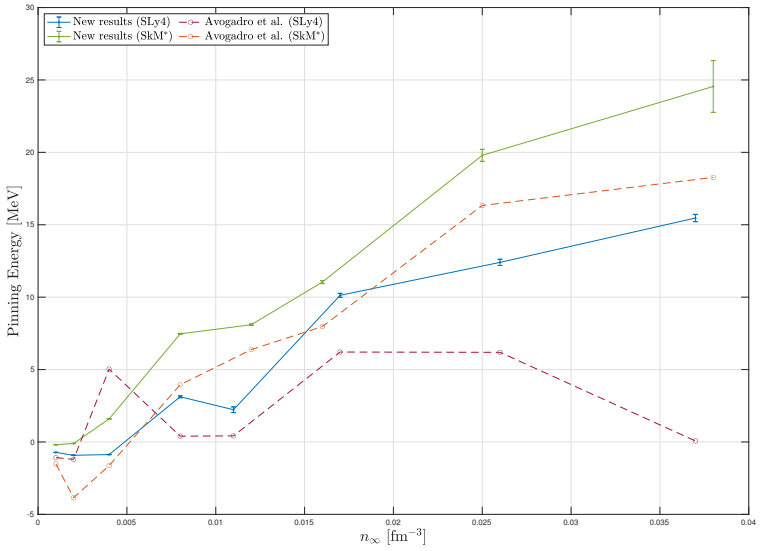

Figure 3.15: The pinning energy as a function of density, compared to the original results of the paper (Avogadro et al., 2008). For each density, the values are estimated using a weighted average of the pinning energies shown in 3.13 and 3.14. The error bars are estimated as prescribed by the weighted mean formula. We present results both for SLy4 and for SkM* interactions.

Chapter 4

Conclusions and prospects

In this thesis, we studied a possible physical mechanism that would potentially explain the observation of sudden spin-ups in neutron star pulsars, known as glitches.

In the inner crust of the star, a sea of superfluid neutrons surrounds a Coulomb lattice of heavy nuclei. Due to the rotation of the star, the superfluid forms an array of vortices threading the neutron sea. These vortices store the superfluid angular velocity whose magnitude depends on the number of vortices per unit area.

The interaction between said vortices and the nuclei in the lattice is thought to be linked to the origin of pulsar glitches. The lattice and the other solid components of the star slow down in time. If vortices are kept in fixed position by their interaction with the nuclei, then the superfluid cannot decelerate, since vortices number cannot change. When a critical difference of angular velocity is reached between the solid and superfluid components of the star, several vortices unpin from their position, releasing their angular momentum to the crust and generating the glitch phenomenon.

The pinning energy is the quantity describing how strongly vortices are repelled or attracted by nuclei. The greater the pinning energy, the bigger the angular momentum released.

In this work, we presented new microscopic estimates for the pinning energy. We build our work on a previous research (Avogadro et al., 2008), where the authors wrote a code that solved Hartree-Fock-Bogolyubov (HFB) equations in a cylindrical box considering a nucleus placed in the centre and a free gas of neutrons surrounding it.

From this starting point, we made various key modifications. While neutrons were considered in axial symmetry in the original work, protons were bound to have spherical symmetry. This was a drawback that has been improved: protons are now considered to be axially symmetric too. As we've found, solving HFB equations for a neutron vortex on top of a nucleus gives rise to appreciable deformations from sphericity.

We also improved numerical aspects of the code. We implemented more precise derivation and integration methods. Numerical accuracy is in fact crucial. The pinning energy, which spans from hundreds of keV to tens of MeV, is the result of a delicate balance of different contributions, each in the order of thousands of MeV. Hence, small numerical errors in the calculations of the

different contributions may entail large errors in the evaluation of the pinning energy. In this regard, we have carefully studied the convergence of our results depending on the size of the cylindrical box and mesh employed to solve the axially symmetric HFB equations.

In our study, we have used two different nuclear effective Hamiltonians, named SLy4 and SkM*, to describe the interaction among neutrons and protons. The results, although quantitatively different, highlight the same trend for both interactions. The pinning energy grows as the density of the surrounding neutron sea grows and it is found to be positive except for the outermost layers of the inner crust we considered. This means that our model favours interstitial pinning almost everywhere, i.e. vortices are repelled by the nuclei and pinned in-between nuclei.

As for the comparison with (Avogadro et al., 2008), their results are qualitatively similar for SkM*, although ours are smoother. On the other hand, the original results for SLy4 showed a peculiar oscillatory behaviour which is remarkably different from our findings.

Even if the new values for the pinning energy are the natural conclusion of our research, there are many ways we can expand our work. First, the inner crust of a neutron star spans densities from $n_\infty \sim 4 \times 10^{11}$ g/cm^3 to $n_\infty \sim 2 \times 10^{14}$ g/cm^3. We investigated only a small portion of the crust; it would be extremely insightful to explore the other regions.

Second, we found pinning energies *per site*, i.e. relative to one nucleus and a very short section of the vortex. Vortices are much longer than the typical dimension of the lattice and they pass through various neutron sea densities. In (Seveso et al., 2016), authors used the pinning energy per site to compute an average force acting on the the entire vortex. It would be compelling to compute such force with our new estimates for the pinning energy.

Finally, we know that at neutron sea densities higher than $n_\infty \sim 4 \times 10^{-2}$ fm^{-3} nuclei enter the so called pasta phase, where strong deformations arise. It is thought that the first of this shape is spaghetti-like, i.e. the nuclei become very thin and elongated. The interaction between a spaghetti nucleus and a vortex, about which we know very little, could be explored and studied with our program in cylindrical symmetry.

To conclude, neutron stars are fascinating object. They exhibit extreme features and are formidable laboratories for exploring phases of matter otherwise inaccessible on Earth. They are expected to be superfluid and glitches could be the direct evidence of the existence of macroscopic superfluid in nature. Our work represent but a small contribution to this evolving and engaging field.

Appendix A

Numerical details

In this appendix we discuss the numerical stability of the code. As we have stated many times, numerical accuracy is very important for this work. Binding energies, the founding blocks of the pinning energies, are computed as the difference between very large numbers (see Section 2.5 and Appendix A).

As we explained in Chapter 2, our program solves HFB equations inside a cylindrical box. Numerically, each quantity (density, pairing gap ...) is defined on a grid (iro,iz), where iro and iz are respectively the index on the ρ and z axis. The parameters $\mathrm{d}\rho$ and $\mathrm{d}z$ determine how distant are two points on the grid.

The box dimensions are set by its height h_{box} and its radius ρ_{box}. In particular, we should ascertain that the program has reached convergence, i.e. the binding energy does not depend on the dimensions of the box.

The results of our calculation cannot clearly depend on such parameters, as it would be unphysical.

We performed three different series of calculations of the binding energy to ascertain that this is in fact the case. We used the SLy4 interaction and put the external neutron density to $n_\infty = 0.001$ fm $^{-3}$. h_{box} is always 40 fm. First we set $\rho_{box} = 30$ fm and $\mathrm{d}\rho = 0.25$ fm and varied $\mathrm{d}z$. Then we set $\rho_{box} = 30$ fm and $\mathrm{d}z = 0.25$ and varied $\mathrm{d}\rho$. Finally, we set $\mathrm{d}\rho = 0.25$ and $\mathrm{d}z = 0.25$ and varied ρ_{box}.

A.1 Variation of $\mathrm{d}z$

We computed the binding energy for three different values of $\mathrm{d}z$: 0.1, 0.2 and 0.25 fm. We set $\rho_{box} = 30$ fm and $\mathrm{d}\rho = 0.25$ fm.

We show in Figure A.1 the results. All results are distant less than one hundred eV, way less than our numerical accuracy (which is in the order of few hundreds of keV). Therefore it is safe to set $\mathrm{d}z = 0.25$ fm for all other calculations.

A.2 Variation of $\mathrm{d}\rho$

We computed the binding energy for six different values of $\mathrm{d}\rho$, spanning from 0.1 fm to 0.5 fm. We set $\rho_{box} = 30$ fm and $\mathrm{d}z = 0.25$ fm.

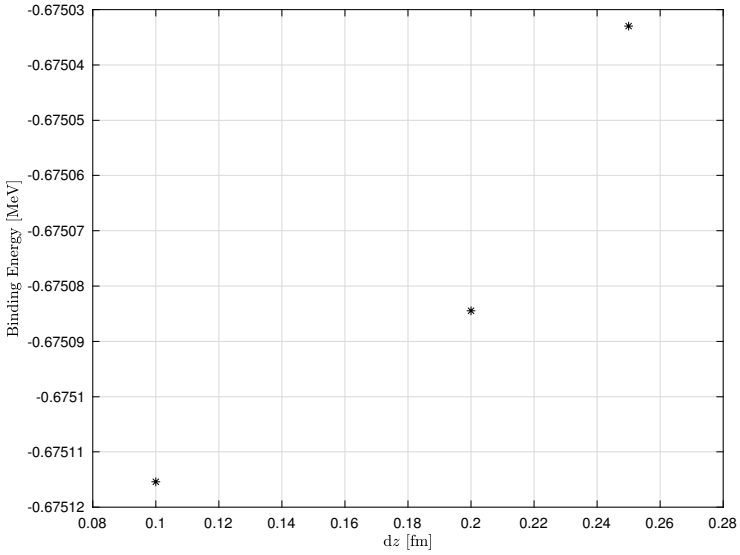

Figure A.1: Binding energy as a function of the z step $\mathrm{d}z$. The results are remarkably close one another and we can safely suppose that the binding energy does not depend on $\mathrm{d}z$.

We show our results in Figure A.2. All results are distant no more than 50 keV.

If we observe the value between 0.3 fm and 0.1 fm, we see that they all lie in a range of 30 keV. Since our uncertainties are in the order of hundreds of keV, we can safely use $\mathrm{d}\rho = 0.25$ fm for all other calculations.

A.3 Variation of ρ_{box}

We computed the binding energy for ten different values of ρ_{box}, spanning from 26 fm to 44 fm. We set $\mathrm{d}\rho = 0.25$ fm and $\mathrm{d}z = 0.25$ fm.

We show our results in Figure A.3. All results are in an interval of approximately 150 keV, which is in the range of our precision. Nonetheless, for values of ρ_{box} lower than 35 fm, we can observe a somewhat oscillatory behaviour. On the other hand, after 35 fm, all the binding energies are in the range of some tens of keV.

We find that it is best to compute binding energies with radii bigger than 35 fm, where we are reasonably sure that convergence has been reached.

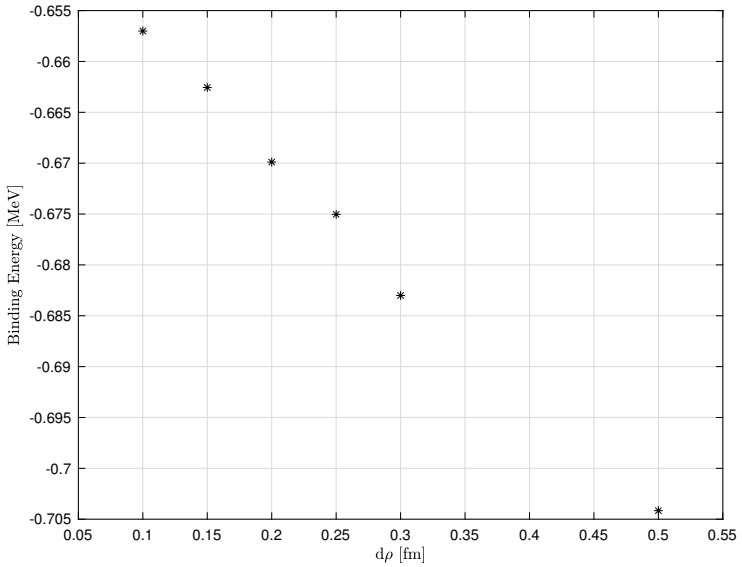

Figure A.2: Binding energy as a function of the ρ step dρ. The results are all within 50 keV; in particular, values below d$\rho = 0.3$ fm are within 30 keV of each other. It is safe to assume then that the binding energy does not depend on dρ.

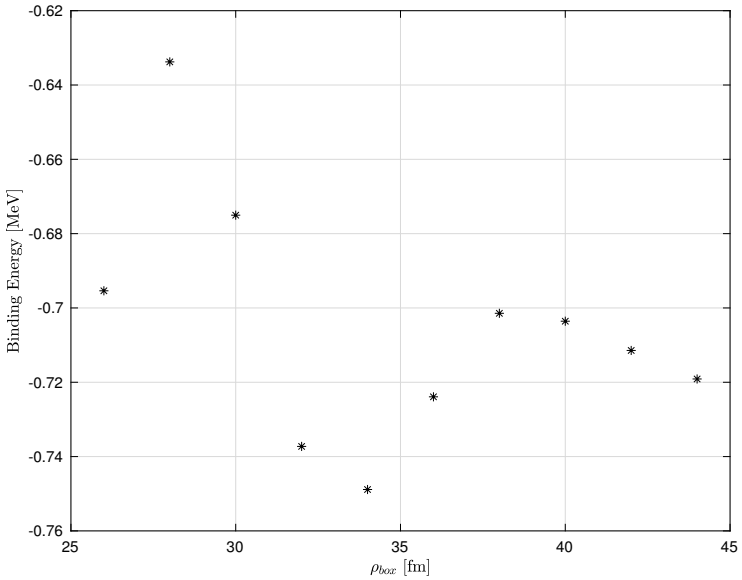

Figure A.3: Binding energy as a function of the box radius ρ_{box}. The results are all within 150 keV, which is approximately our precision. Nonetheless, values for $\rho_{box} > 35$ fm are more stable and reliable.

Appendix B

Calculation details

We present in this appendix all the numerical data needed to compute the pinning energies we have found. We performed calculations for eight different neutron sea densities; for each density we performed three calculations at different values of the box radius ρ_{box}. We used both the SLy4 and SkM* Skyrme-like interactions.

In Table B.1 we show the values of the kinetic correction $K_n(R_{WS})$ at different neutron sea densities, for both interactions.

We report in Tables (B.2 - B.7) the detailed results of each calculation we performed. All the energies are expressed in MeV. E_{tot} is the total energy (pairing plus HF), while N is the number of neutrons. ΔE is the correction that accounts for the small difference in neutron number between the NP an Nu configurations and between the IP and NS configuration. Finally, E_b is the binding energy, given with its error.

n_∞ [fm^{-3}]	$K_n(R_{WS})$ [MeV]	
	SLy4	SkM*
0.001	0.0177 ± 0.0005	0.0168 ± 0.0004
0.002	0.0261 ± 0.0007	0.0317 ± 0.0008
0.004	0.051 ± 0.001	0.052 ± 0.001
0.008	0.105 ± 0.002	0.108 ± 0.003
0.011	0.138 ± 0.004	0.135 ± 0.003
0.017	0.181 ± 0.005	0.159 ± 0.004
0.026	0.217 ± 0.006	0.192 ± 0.005
0.037	0.237 ± 0.006	0.235 ± 0.006

Table B.1: The energy kinetic contribution between vortex and nucleus, at a separation distance R_{WS}.

	SLy4	$\rho_{box} = 38$ fm		
	E_{tot}	N	ΔE	E_b
	$n_\infty = 0.001$ fm^{-3}	$\lambda_n = 1.60$ MeV		
NP	-731.80	243.99	10.93	-0.703 ± 0.005
Nu	-724.79	250.83		
IP	151.27	138.78	11.90	
NS	158.55	146.22		
	$n_\infty = 0.002$ fm^{-3}	$\lambda_n = 2.00$ MeV		
NP	-598.63	315.64	17.20	-0.89 ± 0.01
Nu	-587.71	324.24		
IP	287.55	212.01	18.37	
NS	298.75	221.20		
	$n_\infty = 0.004$ fm^{-3}	$\lambda_n = 3.00$ MeV		
NP	27.84	555.78	43.51	-0.90 ± 0.04
Nu	56.67	570.29		
IP	925.71	456.53	41.05	
NS	951.18	470.22		
	$n_\infty = 0.008$ fm^{-3}	$\lambda_n = 4.70$ MeV		
NP	2709.40	1219.72	101.03	3.18 ± 0.11
Nu	2771.61	1241.22		
IP	3488.15	1091.63	99.23	
NS	3551.76	1112.74		
	$n_\infty = 0.011$ fm^{-3}	$\lambda_n = 5.70$ MeV		
NP	5474.19	1735.61	162.53	3.26 ± 0.10
Nu	5583.00	1764.13		
IP	6293.63	1614.61	144.72	
NS	6387.89	1640.00		
	$n_\infty = 0.017$ fm^{-3}	$\lambda_n = 7.00$ MeV		
NP	11346.23	2634.03	214.18	10.15 ± 0.22
Nu	11477.80	2664.43		
IP	12026.14	2492.31	212.78	
NS	12166.47	2522.72		
	$n_\infty = 0.026$ fm^{-3}	$\lambda_n = 8.50$ MeV		
NP	21824.66	3957.83	375.42	12.80 ± 0.31
Nu	22087.24	4002.00		
IP	22541.19	3820.15	298.32	
NS	22739.47	3855.25		
	$n_\infty = 0.037$ fm^{-3}	$\lambda_n = 10.00$ MeV		
NP	37442.05	5267.38	365.12	13.32 ± 0.30
Nu	37667.15	5663.89		
IP	38052.62	5476.59	336.59	
NS	38262.51	5510.25		

Table B.2: Detailed energies for SLy4 and $\rho_{box} = 38$ fm.

	SLy4	$\rho_{box} = 40$ fm		
	E_{tot}	N	ΔE	E_b
	$n_\infty = 0.001$ fm^{-3}	$\lambda_n = 1.60$ MeV		
NP	-712.64	261.70	11.22	-0.702 ± 0.006
Nu	-705.54	268.71		
IP	170.08	156.30	12.40	
NS	177.66	164.05		
	$n_\infty = 0.002$ fm^{-3}	$\lambda_n = 2.00$ MeV		
NP	-563.87	341.65	18.22	-0.90 ± 0.01
Nu	-532.20	350.76		
IP	322.52	238.21	19.12	
NS	334.30	247.77		
	$n_\infty = 0.004$ fm^{-3}	$\lambda_n = 3.00$ MeV		
NP	137.48	610.35	45.38	-1.34 ± 0.23
Nu	167.63	625.48		
IP	1035.63	511.07	43.16	
NS	1062.22	525.45		
	$n_\infty = 0.008$ fm^{-3}	$\lambda_n = 4.70$ MeV		
NP	3115.42	1347.33	104.27	3.25 ± 0.12
Nu	3179.68	1369.52		
IP	3894.10	1219.25	102.70	
NS	3960.04	1241.10		
	$n_\infty = 0.011$ fm^{-3}	$\lambda_n = 5.70$ MeV		
NP	6201.98	1923.02	166.04	2.37 ± 0.28
Nu	6313.67	1952.15		
IP	7021.07	1801.81	149.44	
NS	7118.53	1828.03		
	$n_\infty = 0.017$ fm^{-3}	$\lambda_n = 7.00$ MeV		
NP	12723.12	2920.19	224.47	10.21 ± 0.24
Nu	12862.93	2952.26		
IP	13405.77	2778.88	220.90	
NS	13552.27	2810.44		
	$n_\infty = 0.026$ fm^{-3}	$\lambda_n = 8.50$ MeV		
NP	24451.06	4400.73	335.05	12.53 ± 0.40
Nu	24670.91	4440.15		
IP	25120.91	4257.57	302.94	
NS	25321.18	4293.21		
	$n_\infty = 0.037$ fm^{-3}	$\lambda_n = 10.00$ MeV		
NP	41682.71	6241.76	461.23	15.97 ± 0.33
Nu	41998.56	6287.88		
IP	42351.16	6097.01	374.56	
NS	42596.31	6134.47		

Table B.3: Detailed energies for SLy4 and $\rho_{box} = 40$ fm.

	SLy4	$\rho_{box} = 42$ fm		
	E_{tot}	N	ΔE	E_b
	$n_\infty = 0.001$ fm^{-3}	$\lambda_n = 1.60$ MeV		
NP	-692.77	280.13	11.61	-0.70 ± 0.01
Nu	-685.42	287.39		
IP	189.88	174.75	12.13	
NS	197.68	182.74		
	$n_\infty = 0.002$ fm^{-3}	$\lambda_n = 2.00$ MeV		
NP	-526.88	369.20	18.90	-0.87 ± 0.01
Nu	-514.77	378.64		
IP	359.42	265.73	19.81	
NS	371.57	275.64		
	$n_\infty = 0.004$ fm^{-3}	$\lambda_n = 3.00$ MeV		
NP	253.50	667.98	46.56	-0.811 ± 0.003
Nu	284.40	683.50		
IP	1151.40	568.80	44.01	
NS	1178.80	583.47		
	$n_\infty = 0.008$ fm^{-3}	$\lambda_n = 4.70$ MeV		
NP	3543.60	1481.80	106.85	3.27 ± 0.12
Nu	3609.40	1504.60		
IP	4312.20	1353.60	105.98	
NS	4389.40	1376.10		
	$n_\infty = 0.011$ fm^{-3}	$\lambda_n = 5.70$ MeV		
NP	6969.00	2120.30	169.57	2.36 ± 0.29
Nu	7082.90	2150.10		
IP	7786.90	1998.90	153.88	
NS	7887.50	2025.90		
	$n_\infty = 0.017$ fm^{-3}	$\lambda_n = 7.00$ MeV		
NP	14178.82	3222.33	230.84	10.58 ± 0.24
Nu	14322.76	3255.31		
IP	14862.03	3081.17	225.47	
NS	15011.19	3113.38		
	$n_\infty = 0.026$ fm^{-3}	$\lambda_n = 8.50$ MeV		
NP	27140.52	4858.24	367.52	12.39 ± 0.43
Nu	27390.56	4901.48		
IP	27833.49	4717.79	312.34	
NS	28040.74	4754.54		
	$n_\infty = 0.037$ fm^{-3}	$\lambda_n = 10.00$ MeV		
NP	46270.04	6901.34	439.30	15.35 ± 0.38
Nu	46561.80	6945.27		
IP	46933.12	6755.98	357.66	
NS	47158.59	6791.74		

Table B.4: Detailed energies for SLy4 and $\rho_{box} = 42$ fm.

	SkM*	$\rho_{box} = 38$ fm		
	E_{tot}	N	ΔE	E_b
	$n_\infty = 0.001$ fm^{-3}	$\lambda_n = 1.25$ MeV		
NP	-796.50	256.77	16.63	-0.16 ± 0.01
Nu	-784.42	270.63		
IP	132.38	151.52	15.61	
NS	143.29	164.54		
	$n_\infty = 0.002$ fm^{-3}	$\lambda_n = 1.35$ MeV		
NP	-736.76	301.27	22.26	-0.05 ± 0.01
Nu	-720.24	318.01		
IP	193.68	197.11	20.44	
NS	207.98	212.25		
	$n_\infty = 0.004$ fm^{-3}	$\lambda_n = 2.00$ MeV		
NP	-260.33	566.28	75.58	1.64 ± 0.01
Nu	-200.85	604.07		
IP	680.10	467.48	49.63	
NS	715.26	492.30		
	$n_\infty = 0.008$ fm^{-3}	$\lambda_n = 3.00$ MeV		
NP	1515.76	1230.07	112.42	7.54 ± 0.05
Nu	1597.02	1270.88		
IP	2398.78	1105.98	111.65	
NS	2476.81	1143.20		
	$n_\infty = 0.012$ fm^{-3}	$\lambda_n = 3.52$ MeV		
NP	2980.73	1653.07	170.52	8.24 ± 0.08
Nu	3096.79	1701.37		
IP	3889.35	1535.61	146.38	
NS	3989.51	1577.08		
	$n_\infty = 0.016$ fm^{-3}	$\lambda_n = 4.20$ MeV		
NP	5438.34	2255.01	246.28	11.20 ± 0.16
Nu	5609.81	2313.64		
IP	6377.10	2144.06	186.51	
NS	6500.01	2188.47		

Table B.5: Detailed energies for SkM* and $\rho_{box} = 38$ fm. As explained in Section 3.5, we do not show the results for $n_\infty = 0.025$ fm^{-3} and $n_\infty = 0.038$ fm^{-3}, since they are not reliable.

	SkM*	$\rho_{box} = 40$ fm		
	E_{tot}	N	ΔE	E_b
	$n_\infty = 0.001$ fm^{-3}	$\lambda_n = 1.25$ MeV		
NP	-779.08	276.89	17.16	-0.17 ± 0.01
Nu	-766.66	291.19		
IP	149.68	171.56	16.30	
NS	161.06	185.14		
	$n_\infty = 0.002$ fm^{-3}	$\lambda_n = 1.35$ MeV		
NP	-712.24	326.60	23.89	-0.08 ± 0.01
Nu	-694.66	344.30		
IP	218.64	222.78	21.30	
NS	233.54	238.56		
	$n_\infty = 0.004$ fm^{-3}	$\lambda_n = 2.00$ MeV		
NP	-176.60	624.29	78.06	1.64 ± 0.02
Nu	-115.19	663.32		
IP	764.08	525.65	51.78	
NS	800.85	551.54		
	$n_\infty = 0.008$ fm^{-3}	$\lambda_n = 3.00$ MeV		
NP	1802.86	1363.04	126.60	7.59 ± 0.05
Nu	1887.10	1405.24		
IP	2685.78	1238.96	115.94	
NS	2767.00	1277.61		
	$n_\infty = 0.012$ fm^{-3}	$\lambda_n = 3.52$ MeV		
NP	3439.98	1835.28	176.71	8.21 ± 0.10
Nu	3560.75	1885.34		
IP	4349.61	1718.13	151.63	
NS	4453.50	1761.08		
	$n_\infty = 0.016$ fm^{-3}	$\lambda_n = 4.20$ MeV		
NP	6184.35	2506.83	253.07	11.19 ± 0.19
Nu	6360.62	2567.08		
IP	7123.59	2396.05	192.67	
NS	7250.66	2441.92		

Table B.6: Detailed energies for SkM* and $\rho_{box} = 40$ fm. As explained in Section 3.5, we do not show the results for $n_\infty = 0.025$ fm^{-3} and $n_\infty = 0.038$ fm^{-3}, since they are not reliable.

SkM*	$\rho_{box} = 42$ fm			
	E_{tot}	N	ΔE	E_b
	$n_\infty = 0.001$ fm^{-3}	$\lambda_n = 1.25$ MeV		
NP	-761.11	297.72	17.88	-0.19 ± 0.01
Nu	-48.11	312.62		
IP	167.80	192.58	16.84	
NS	179.57	206.62		
	$n_\infty = 0.002$ fm^{-3}	$\lambda_n = 1.35$ MeV		
NP	-686.12	353.42	24.74	-0.07 ± 0.01
Nu	-667.90	371.75		
IP	244.70	249.65	22.08	
NS	260.18	266.01		
	$n_\infty = 0.004$ fm^{-3}	$\lambda_n = 2.00$ MeV		
NP	-87.91	685.58	79.50	1.66 ± 0.02
Nu	-25.55	725.33		
IP	852.33	586.78	53.54	
NS	890.39	613.56		
	$n_\infty = 0.008$ fm^{-3}	$\lambda_n = 3.00$ MeV		
NP	2105.32	1503.10	130.06	7.61 ± 0.06
Nu	2191.98	1546.46		
IP	2987.50	1378.81	119.82	
NS	3071.53	1418.75		
	$n_\infty = 0.012$ fm^{-3}	$\lambda_n = 3.52$ MeV		
NP	3925.05	2027.54	180.93	8.23 ± 0.10
Nu	4048.67	2078.80		
IP	4833.65	1910.12	156.59	
NS	4941.15	1954.48		
	$n_\infty = 0.016$ fm^{-3}	$\lambda_n = 4.20$ MeV		
NP	6970.37	2772.13	258.71	11.22 ± 0.20
Nu	7150.47	2833.73		
IP	7908.95	2661.19	198.74	
NS	8040.30	2708.51		
	$n_\infty = 0.025$ fm^{-3}	$\lambda_n = 5.60$ MeV		
NP	15947.76	4520.44	298.38	20.00 ± 0.41
Nu	16110.63	4572.00		
IP	16840.36	4398.03	297.51	
NS	16996.93	4444.90		
	$n_\infty = 0.038$ fm^{-3}	$\lambda_n = 7.50$ MeV		
NP	32682.11	7002.69	253.07	24.7 ± 1.8
Nu	32808.76	7042.47		
IP	33545.87	6872.52	192.67	
NS	33696.43	6912.19		

Table B.7: Detailed energies for SkM* and $\rho_{box} = 42$ fm.

Bibliography

Anderson, P. W. and N. Itoh (1975). "Pulsar glitches and restlessness as a hard superfluidity phenomenon". In: Nature 256.5512, pp. 25–27. DOI: 10.1038/256025a0.

Avogadro, P. et al. (2008). "Vortex nucleus interaction in the inner crust of neutron stars". In: Nucl. Phys. A 811.3-4, pp. 378–412. DOI: 10.1016/j.nuclphysa.2008.07.010. arXiv: 0804.1765 [astro-ph].

Baldo, M. et al. (2005). "The role of superfluidity in the structure of the neutron star inner crust". In: Nucl. Phys. A 750.2, pp. 409–424. DOI: 10.1016/j.nuclphysa.2005.01.004.

Bartel, J. et al. (1982). "Towards a better parametrisation of Skyrme-like effective forces: A critical study of the SkM force". In: Nucl. Phys. A 386.1, pp. 79–100. DOI: 10.1016/0375-9474(82)90403-1.

Boynton, P. E. et al. (1972). "Optical Timing of the Crab Pulsar, NP 0532". In: ApJ 175, p. 217. DOI: 10.1086/151550.

Bulgac, Aurel, Michael McNeil Forbes, and Rishi Sharma (2013). "Strength of the Vortex-Pinning Interaction from Real-Time Dynamics". In: Phys. Rev. Lett. 110.24, 241102, p. 241102. DOI: 10.1103/PhysRevLett.110.241102. arXiv: 1302.2172 [nucl-th].

Chabanat, E. et al. (1997). "A Skyrme parametrization from subnuclear to neutron star densities". In: Nucl. Phys. A 627, pp. 710–746. DOI: 10.1016/S0375-9474(97)00596-4.

— (1998a). "A Skyrme parametrization from subnuclear to neutron star densities Part II. Nuclei far from stabilities". In: Nucl. Phys. A 635.1-2, pp. 231–256. DOI: https://doi.org/10.1016/S0375-9474(98)00180-8.

— (1998b). "Erratum to "A Skyrme parametrization from subnuclear to neutron star densities. (II): Nuclei far from stabilities" [Nucl. Phys. A 635 (1998) 231-256]". In: Nucl. Phys. A 643.4, pp. 441–441. DOI: 10.1016/S0375-9474(98)00570-3.

Colò, Gianluca and Xavier Roca-Maza (2021). *User guide for the hfbcs-qrpa(v1) code*. arXiv: 2102.06562 [nucl-th].

Discover. https://www.discovermagazine.com/technology/getting-to-know-pulsars-the-lighthouses-of-the-cosmos.

Donati, Paola and Pierre M. Pizzochero (2004). "Fully consistent semi-classical treatment of vortex-nucleus interaction in rotating neutron stars". In: Nucl. Phys. A 742.3-4, pp. 363–379. DOI: 10.1016/j.nuclphysa.2004.07.002.

— (2006). "Realistic energies for vortex pinning in intermediate-density neutron star matter". In: *Physics Letters B* 640.3, pp. 74–81. DOI: 10.1016/j.physletb.2006.07.047.

Downs, G. S. (1981). "JPL pulsar timing observations. I. The VELA pulsar." In: ApJ 249, pp. 687–697. DOI: 10.1086/159330.

Epstein, Richard I. and Gordon Baym (1988). "Vortex Pinning in Neutron Stars". In: ApJ 328, p. 680. DOI: 10.1086/166325.

Espinoza, C. M. et al. (2011). "A study of 315 glitches in the rotation of 102 pulsars". In: MNRAS 414.2, pp. 1679–1704. DOI: 10.1111/j.1365-2966.2011.18503.x. arXiv: 1102.1743 [astro-ph.HE].

Garrido, E. et al. (1999). "Effective density-dependent pairing forces in the T=1 and T=0 channels". In: Phys. Rev. C 60.6, 064312, p. 064312. DOI: 10.1103/PhysRevC.60.064312. arXiv: nucl-th/9909026 [nucl-th].

Gygi, François and Michael Schlüter (1991). "Self-consistent electronic structure of a vortex line in a type-II superconductor". In: Phys. Rev. B 43.10, pp. 7609–7621. DOI: 10.1103/PhysRevB.43.7609.

Lohsen, E. (1975). "Third speed-up of the Crab pulsar". In: Nature 258.5537, pp. 688–689. DOI: 10.1038/258688a0.

Lounasmaa, Olli V. and Erkki Thuneberg (1999). "Vortices in Rotating Superfluid ^{3}He". In: *Proceedings of the National Academy of Science* 96.14, pp. 7760–7767. DOI: 10.1073/pnas.96.14.7760.

Magnus Effect. https://www.norwegiancreations.com/2019/02/the-magnus-effect/.

McCulloch, P. M. et al. (1981). "PSR 0833-45". In: IAU Circ. 3644, p. 2.

Negele, J. W. and D. Vautherin (1973). "Neutron star matter at sub-nuclear densities". In: Nucl. Phys. A 207.2, pp. 298–320. DOI: 10.1016/0375-9474(73)90349-7.

Pulsar glitches. http://www.jb.man.ac.uk/pulsar/glitches.html. Accessed: 2010-09-30.

Seveso, S. et al. (2016). "Mesoscopic pinning forces in neutron star crusts". In: MNRAS 455.4, pp. 3952–3967. DOI: 10.1093/mnras/stv2579.

Shapiro, Stuart L. and Saul A. Teukolsky (2004). *Black holes, white dwarfs and neutron stars*. Wiley-VCH. DOI: 10.1002/9783527617661.

Wikipedia. https://commons.wikimedia.org/wiki/File:Neutron_star_cross_section.svg.

Younes, Walid, Daniel Marc Gogny, and Jean-François Berger (2019). *A Microscopic Theory of Fission Dynamics Based on the Generator Coordinate Method*. Vol. 950. DOI: 10.1007/978-3-030-04424-4.

Yu, Yongle and Aurel Bulgac (2003). "Spatial Structure of a Vortex in Low Density Neutron Matter". In: Phys. Rev. Lett. 90.16, 161101, p. 161101. DOI: 10.1103/PhysRevLett.90.161101. arXiv: nucl-th/0212072 [nucl-th].